Haverford College

Haverford Scholarship

Faculty Publications

Astronomy

2009

Spectral energy distribution of radio sources in nearby clusters of galaxies: implications for Sunyaev-Zel'dovich effect surveys

Yen-Ting Lin

Bruce Partridge
Haverford College, bpartrid@haverford.edu

J. C. Pober '07
Class of 2007, Haverford College

Khadija El Bouchefry

Sarah Burke '06
Class of 2006, Haverford College

See next page for additional authors

Follow this and additional works at: https://scholarship.haverford.edu/astronomy_facpubs

Repository Citation

Authors

Yen-Ting Lin, Bruce Partridge, J. C. Pober '07, Khadija El Bouchefry, Sarah Burke '06, Jonathan N. Klein '08, and Joseph Coish '09

2009

Spectral energy distribution of radio sources in nearby clusters of galaxies: implications for Sunyaev-Zel'dovich effect surveys

Yen-Ting Lin

R. Bruce Partridge
Haverford College

J. C. Pober '07
Class of 2007, Haverford College

Khadija El Bouchefry

Sarah Burke '06
Class of 2006, Haverford College

See next page for additional authors

Repository Citation

Authors
Yen-Ting Lin, R. Bruce Partridge, J. C. Pober '07, Khadija El Bouchefry, Sarah Burke '06, Jonathan N. Klein '08, and Joseph Coish '09

SPECTRAL ENERGY DISTRIBUTION OF RADIO SOURCES IN NEARBY CLUSTERS OF GALAXIES: IMPLICATIONS FOR SUNYAEV–ZEL'DOVICH EFFECT SURVEYS

Yen-Ting Lin[1,2,8], Bruce Partridge[3], J. C. Pober[3], Khadija El Bouchefry[3,4], Sarah Burke[3,5], Jonathan N. Klein[3],
Joseph W. Coish[3], and Kevin M. Huffenberger[6,7]

[1] Princeton University Observatory, Princeton, NJ 08544, USA; yen-ting.lin@ipmu.jp
[2] Departamento de Astronomía y Astrofísica, Pontificia Universidad Católica de Chile, Chile
[3] Department of Astronomy, Haverford College, Haverford, PA 19041, USA; bpartrid@haverford.edu
[4] Astrophysics and Cosmology Research Unit, University of KwaZulu-Natal, South Africa
[5] Swinburne University of Technology, Australia
[6] Jet Propulsion Laboratory, California Institute of Technology, Pasadena, CA 91109, USA
[7] Department of Physics, University of Miami, Coral Gables, FL 33146, USA
Received 2008 May 13; accepted 2009 January 6; published 2009 March 20

ABSTRACT

To explore the high-frequency radio spectra of galaxies in clusters, we used NRAO's Very Large Array at four frequencies, 4.9–43 GHz, to observe 139 galaxies in low redshift ($z < 0.25$), X-ray detected, clusters. The clusters were selected from the survey conducted by Ledlow and Owen, who provided redshifts and 1.4 GHz flux densities for all the radio sources. We find that more than half of the observed sources have steep microwave spectra as generally expected ($\alpha < -0.5$, in the convention $S \propto \nu^\alpha$). However, 60%–70% of the unresolved or barely resolved sources have flat or inverted spectra. Most of these show an upward turn in flux at $\nu > 22$ GHz, implying a higher flux than would be expected from an extrapolation of the lower-frequency flux measurements. Our results quantify the need for careful source subtraction in increasingly sensitive measurements of the Sunyaev–Zel'dovich effect in clusters of galaxies (as currently being conducted by, for instance, the Atacama Cosmology Telescope and South Pole Telescope groups).

Key words: galaxies: active – galaxies: clusters: general – galaxies: elliptical and lenticular, cD – radio continuum: galaxies

Online-only material: color figures

1. INTRODUCTION

The Sunyaev–Zel'dovich effect (SZE; Sunyaev & Zel'dovich 1970) is a powerful method for detecting clusters from observations of the cosmic microwave background (CMB). The hot electrons in the intracluster medium (ICM) inverse-Compton scatter the CMB photons, distorting the CMB spectrum as seen in the direction of a cluster. Because the SZE is redshift independent and is caused by the presence of dense gas deep within the potential well of dark matter halos, SZE surveys can effectively detect high-redshift clusters (see e.g., Carlstrom et al. 2002, for a recent review) and are less confused by large-scale structure than optical surveys.

Several microwave background experiments with mJy level sensitivity and 1′–10′ beams, including the Atacama Cosmology Telescope (ACT[9]; Fowler et al. 2007), the South Pole Telescope (SPT[10]; Staniszewski et al. 2008; Ruhl et al. 2004), the Arcminute Microkelvin Imager (AMI[11]; Zwart et al. 2008; AMI Collaboration 2006), the Atacama Pathfinder Experiment SZ survey (APEX-SZ[12]), and *Planck*[13], will yield thousands of SZE clusters in the next few years; in particular, all four ground experiments were already operational in 2007. The data from these surveys will permit the study of the mass function of clusters over cosmic epochs, a measurement which can elucidate

the role of dark energy because structure growth slows during dark energy domination.

As a probe of precision cosmology, an SZE survey has to control its systematics, particularly regarding the correlation between the SZE signal and cluster mass (e.g., Lin & Mohr 2003). Radio point sources often found at or near cluster centers pose serious challenges in this regard (Carlstrom et al. 2002). Powerful sources can overwhelm the cluster SZE signature (Cooray et al. 1998; Coble et al. 2007), and weaker, unresolved sources can collectively contaminate the SZE signal (Pierpaoli & Perna 2004). Clusters missed or affected this way would distort the measurements of cosmological parameters from SZE surveys, and it is therefore crucial to estimate the degree of contamination due to radio sources.

Although at low frequencies (1.4–5 GHz) there have been extensive studies of the radio galaxy population in clusters (e.g., Ledlow & Owen 1996; Miller & Owen 2001; Morrison & Owen 2003; Lin & Mohr 2007), it is not clear at present how these sources behave at the frequencies ($\geqslant 15$ GHz) and flux levels ($\sim$mJy) of ongoing SZE surveys. Most of the forecasts for future surveys therefore rely on large extrapolations either in frequency or in flux level, and often both, from existing data (e.g., Toffolatti et al. 1998; Knox et al. 2004; White & Majumdar 2004; de Zotti et al. 2005; however, see Sadler et al. 2008 for recent observations at 95 GHz). For example, Lin & Mohr (2007, hereafter LM07) use the observed spectral energy distribution (SED) and spectral index distribution (SID) from 1.4 to 4.85 GHz to estimate SZE survey contamination from the observed 1.4 GHz cluster radio luminosity function (RLF). At 150 GHz, they estimate that about 10% of the clusters of mass 10^{14}–10^{15} $M_\odot$ may host active galactic nuclei (AGNs)

---

[8] Current address: Institute for the Physics and Mathematics of the Universe, University of Tokyo, Japan.
[9] www.physics.princeton.edu/act/index.html
[10] pole.uchicago.edu/
[11] www.mrao.cam.ac.uk/telescopes/ami/index.php
[12] bolo.berkeley.edu/apexsz/
[13] www.rssd.esa.int/Planck/

whose total fluxes exceed that of the SZE signal. Although the AGN contribution can be detected and subtracted by combining observations at different frequencies used in an SZE survey, a more critical issue is to be able to quantify the uncertainty about the fraction of clusters being lost or contaminated at few percent level (Lima & Hu 2005). This extrapolation over 2 orders of magnitude in frequency (i.e., from 1.4 GHz to 150 GHz) is highly uncertain, and points out the importance of understanding the actual frequency dependence of these cluster sources.

An extensive follow-up of the 15 GHz 9C survey from 1.4 to 43 GHz (Bolton et al. 2004) clearly demonstrates that the SED of radio sources is highly nontrivial, but does not focus on cluster radio sources. With sensitive observations toward 89 clusters over $0.1 \leqslant z < 1$, Coble et al. (2007) determined the SID between 1.4 and 28.5 GHz. This is a major step toward understanding of the nature of the radio sources in intermediate- to high-z clusters. However, we note that their sample is effectively selected against clusters hosting bright radio sources. Furthermore, only a few of the radio sources are spectroscopically confirmed cluster members. Therefore, it is not clear whether their sample is representative of the cluster radio source population as a whole.

Here, we present a systematic study of the SED of *cluster* radio sources from 4.86 to 43.3 GHz, conducted with the Very Large Array (VLA). 139 radio galaxies associated with 110 clusters at $z < 0.25$ are observed at three or four frequency bands *nearly simultaneously*, allowing better determination of the spectral shape. Photometric data from the Sloan Digital Sky Survey (SDSS), where available, are used to examine the correlations (if any) between the SID/SED and the properties of the host galaxy and cluster, such as color, luminosity, and clustercentric distance. Our survey improves upon previous studies in several aspects, including the selection of cluster member galaxies based on available redshifts, the large sample size, and the near-simultaneous measurement of fluxes in all four bands.

This paper is organized as follows. In Section 2, we describe our cluster and radio galaxy sample. The details of the observations and data reduction are provided in Sections 3 and 4, respectively. As the angular resolution of the observations at different frequencies is quite different, we pay particular attention in comparing the fluxes in different bands; the procedure is reported in Section 5. We present the SED and SID of the sources in Section 6, and the properties of the host galaxies and clusters in Section 7. Based on these new results, we forecast the possible contamination due to radio sources of SZE surveys in Section 8. We conclude by summarizing our main findings and suggesting directions for further work in Section 9.

Throughout this paper, we employ a flat lambda cold dark matter (ΛCDM) cosmological model where $\Omega_M = 1 - \Omega_\Lambda = 0.3$ and $H_0 = 70 \ h_{70}$ km s^{-1} Mpc^{-1}.

2. CLUSTER AND RADIO GALAXY SAMPLE SELECTION

Ledlow & Owen conducted a 1.4 GHz survey of radio galaxies in ~400 clusters at $z < 0.25$ with a limiting sensitivity of 10 mJy, and provided extensive redshift measurements for the host galaxies (Ledlow & Owen 1995, 1996; Owen et al. 1995; Owen & Ledlow 1997). Their cluster sample was drawn from the Abell catalogs (Abell 1958), and was restricted to area with reddening at the *R*-band of less than 0.1 mag. We further limited ourselves to 110 clusters that are detected in X-rays. The main reasons for this requirement are (1) as our ultimate goal is to

make predictions for the radio source contamination in SZE surveys, it is preferable to work with a cluster sample that is selected in a similar fashion as in SZE surveys; and (2) the X-ray emission provides a rough estimate of the cluster mass, which is an important ingredient in our forecast for the SZE surveys. As radio galaxies are rare, to maximize the sample size, we did not set any X-ray flux limit as we compiled our cluster sample. Based on Ledlow & Owen's redshift catalog, 139 galaxies associated with these clusters were selected as our radio galaxy sample.

We note that Ledlow & Owen (1995, 1996; see also Owen et al. 1995; Owen & Ledlow 1997) surveyed the galaxies within 0.3 Abell radius of the cluster center (i.e., ≈0.64 h_{70}^{-1} Mpc), irrespective of the size (mass) of the clusters. Given the high concentration in the spatial distribution of radio sources within clusters (LM07), their approach should include the majority of the sources associated with the clusters, thus providing us with a representative initial sample of radio galaxies. Using only sources projected within 40% of the virial radius does not change the derived SIDs or forecasts on the radio source contamination of the SZE (see Sections 7 and 8).

In some cases, we detect galaxies not in our initial sample that we could confirm are cluster members on the basis of common redshift (see Section 6.1).

3. OBSERVATIONS

Measurements in all four spectral bands were made at default VLA frequencies, centered at 43.3, 22.4, 8.5, and 4.9 GHz.[14] The observations discussed here were made in late 2005 October, with the VLA in a hybrid DnC configuration. In this configuration, the north–south baselines are on average longer than the east–west baselines, and as a consequence the synthesized beam is highly elliptical except for sources observed near the meridian at low elevation. During our runs, several antennas had been removed for repair or refitting; on average we had only 22 available, resulting in a ~20% reduction in sensitivity from the full array of 27. The first run, during the night October 23–24, was carried out in mostly cloudy weather with poor atmospheric phase stability. We consequently elected to defer the 43 GHz observations to later runs. The high-frequency *Q*-band observations were concentrated in a short run on October 28 and a much longer run on October 29–30— the latter in excellent, clear weather. The final short run on the night of October 31 was used to obtain fill-in measurements on sources missed earlier at various frequencies.

3.1. Calibration

For all but the October 31 run, our flux density scale was based on 1331+305 (3C286), for which NRAO specifies flux densities of 1.4554, 2.5192, 5.205, and 7.485 Jy at 43.3, 22.4, 8.5, and 4.9 GHz, respectively. 3C286 was not visible during our short run on October 31; for these data we employed 3C48 as the primary flux calibrator, and carefully intercompared the flux densities obtained for sources and secondary calibrators observed in common on this day and earlier ones. In the case of the two highest frequency bands, we employed standard software in the AIPS software package to import a model of the primary calibrators to take account of slight resolution effects in the *K* and *Q* bands.

---

[14] Throughout this paper we refer to these frequency bands as *Q*, *K*, *X*, and *C* bands, respectively. Note that the 1.4 GHz channel is denoted as the *L* band.

Table 1
Instrumental Parameters

Frequency (GHz)	Integration Time (s)	Typical Image Sensitivity (mJy)	Image Pixel Size (arcsec)	Synthesized Beam (approx.)
4.86	80	2.0	1.0	$8'' \times 13''$
8.46	50	0.5	0.6	$4'' \times 8''$
22.46	120	1.0	0.2	$2'' \times 3''$
43.34	$\sim$300[a]	0.8	0.2[b]	$2'' \times 3''$[b]

Notes.
[a] Fast switching employed (see Section 3.2).
[b] For tapered images (see Section 5.1).

A variety of secondary (phase) calibrators were employed; we in general selected calibrator sources with reasonably flat spectra so that the same source could be used for observations in all four bands. Calibrators generally were within $\sim$15° of all of our cluster sources.

Additional information on some instrumental parameters is provided in Table 1. Note that the values for the synthesized beam shape are approximate, since the beam geometry depends on the declination and hour angle of the source.

3.2. Fast Switching

In the case of the 43 GHz observations, we employed fast switching between the source of interest and a nearby phase calibrator source. The integration times on source and calibrator were set to be approximately equal to or less than the atmospheric phase coherence time at 43 GHz. Rather than adjusting these integration times on the fly, we set them to be 100 s on sources between calibrations, and 40 s on nearby calibrators. For each galaxy observed, this cycle was repeated 3 times.

4. DATA REDUCTION, ANALYSIS, AND IMAGING

The raw amplitude and phase data are flagged for shadowing of one antenna by another, interference, noisy correlators, weak antennas, and so on. In general, this flagging process removes only a few percent of the raw data. When data from the available antennas in the array are combined, the data are weighted by the inverse of the variance in the average signal.

Each source at each of the four frequencies is imaged using standard NRAO procedures in the AIPS software package. In forming the images, the pixel or cell size initially employed is $0''.1$, $0''.2$, $0''.6$, and $1''.0$ at 43.3, 22.5, 8.5, and 4.9 GHz, respectively. These values allow complete sampling of the synthesized beam even along its minor axis. In all cases, we make 1024^2 images. The raw images are lightly cleaned of side lobes ($\sim$200 iterations) again using standard NRAO procedures in AIPS. In most cases, when a source or sources are evident in the raw image, we clean first in a small area containing the source(s), then lightly clean the entire 1024^2 pixel image. If no source is evident in the initial image, we simply clean lightly over the entire area. We have experimented with different levels of cleaning, and found no significant change in the flux densities of sources.

4.1. Flux Density of Unresolved or Barely Resolved Sources

Flux densities of evident, and unresolved or barely resolved, sources are determined by fitting a two-dimensional Gaussian to each image, using a standard process in AIPS (specifically, IMFIT). We report the integrated flux for each source. When no

source is evident at or near the specified position, we compare 4σ (σ is the local noise rms) to 2σ added onto the brightest flux per beam near the image center (within 50 pixels), and present the larger of the two as an upper limit.

5. EFFECTS OF RESOLUTION

As expected, many cluster radio sources show evident, resolved, structure at one or more of our observing frequencies. For resolved or irregular sources it is more difficult to obtain accurate fluxes; more importantly, the flux densities of resolved and complex sources are difficult to compare at different frequencies. For instance, the lobes of some of the classical FRII radio sources in our list are well delineated at 4.9 GHz, but only isolated hot spots in the lobes are visible at higher frequencies. In addition, the angular resolution of the VLA-synthesized beam in the DnC configuration varies from $\sim$2'' to $\sim$13'' depending on frequency; much of the flux of extended sources is resolved out at higher frequencies. When flux is resolved out, only lower limits can be placed on spectral indices.

5.1. Tapered 43 GHz Images

Since we are most interested in the highest frequencies, 22 and 43 GHz, flux densities and the 22–43 GHz spectral index, we convolve our 43 GHz images with an elliptical Gaussian weighting profile to broaden the synthesized beam to match approximately the larger size of the synthesized beam at 22 GHz. This is done by applying a Gaussian weighting function to the $u - v$ data before imaging, again using a standard procedure in the AIPS task IMAGR. A $u - v$ taper of $45k\lambda$ and $135k\lambda$ provides a good overall match to the 22 GHz beam. For these tapered images we employ $0''.2$ cells, as for the 22 GHz images. By approximately matching the 22 and 43 GHz synthesized beams, we eliminate or reduce the problem of resolution and are able to compare fluxes from matched areas of the sky. Thus, our 22–43 GHz spectral indices are unbiased values.

Unless otherwise noted, all flux densities at 43 GHz are derived from these tapered images.

Because of the larger frequency ratio between 8.5 and 22 GHz, tapering the 22 GHz images to match the 8.5 GHz synthesized beam produces very noisy images (much of the $u - v$ data was strongly downweighted), so we elect not to taper the 22 GHz images; see Section 6.4 for further details. Hence spectral indices based on fluxes at 8.5 (or 4.9) GHz are lower limits, as noted above.

5.2. Flux Density of Resolved or Irregular Sources

In the case of irregularly shaped or clearly extended sources, we estimate the flux density within a rectangular region including all of the visible emission. These are figures cited in

Table 2
Detection Statistics

Detection[a]	All Morphologies		Core/Pointlike	
	Components	Galaxies	Components	Galaxies
All 4	87	75	57	57
$\geqslant 3$	140	111	73	73
$\geqslant 2$	185	133	83	83
$\geqslant 1$	192	136	86	85
Total	195[b]	139[b]	86	85

Notes.
[a] Number of bands in which the sources are detected.
[b] Three sources detected at 1.4 GHz by Owen & Ledlow (1997) were not detected at any frequency in our VLA observations.

Table 3 (see Section 6). Relatively few of the 22 and 43 GHz sources are complex enough to require this treatment.

6. OBSERVATIONAL RESULTS

We have observed 139 galaxies, and detected 136 in at least one band. The three that show no sign of a source at any of the frequencies are 0053−102B, 1108+410A, and 1657+325B. These three are not included in our analysis. We note that the first and last of these three are weak 21 cm sources in Ledlow & Owen's catalog. On the other hand, 1108+410A has a flux of 116 mJy in their catalog, but is very extended. In our 4.9 GHz image, we see faint traces of a source, but it is almost entirely resolved out even at $\sim 12''$ resolution.

For 111 galaxies we are able to measure flux in at least three bands. This subsample will allow better determination of the spectral shape, and will be the focus of this section. Some of these galaxies have multiple components, and in total we detect 140 radio sources associated with them. Table 2 records the detection statistics of our sources. In Table 3, we provide the available flux density measurements of all the sources. Most blank entries in Table 3 are for background sources (see Section 6.1) far enough from the image centers so that they are not contained within the primary beams at the two higher frequencies we employed. In other cases, our runs on a particular source at a particular frequency were spoiled by weather or lost for other reasons. In a smaller number of cases, including for instance 0816+526, sources seen independently at the higher frequencies were blended at 5 GHz, so that it was not possible to determine accurate flux densities at that frequency.

6.1. "Background" Sources

In many of our images, especially those at low frequencies with their correspondingly larger solid angle, we by chance detect sources at a distance from the center of the field (or pointing position). Since our target galaxies are all at low redshift, these peripheral sources are presumably mostly background radio sources. We exclude from our analysis of the statistical properties of cluster radio galaxies all such "background" sources. Four of these "background" sources, however, have cataloged redshifts which show they are cluster members. These four are added to our sample of cluster galaxies in the subsequent analysis.

6.2. Overall Properties of Cluster Radio Galaxies

We now focus on the 111 cluster radio galaxies for which the spectral shape can be reliably traced, since we have measurements at $\geqslant 3$ frequencies. At the lowest frequency, 4.9 GHz,

virtually all of the sources have complex structure. In $\sim 75\%$ of the sources, a clear core or small, barely resolved jet is visible. Even in these cases, however, there is generally additional extended emission. In other sources, the cores or other resolved or barely resolved structures visible in higher frequency, higher resolution, images are unresolved or merged with diffuse structure in the 4.86 GHz images. An example is shown in Figure 1. This makes it difficult to isolate the cores at our lowest frequency, and to determine their flux densities for comparison with measurements at higher frequencies. In some cases, our best option is to compare the 4.9 GHz flux of an entire source with the sum of the flux densities of its components at the next highest frequency.

At the next highest frequency, 8.5 GHz, with a $4'' \times 8''$ beam, cores and jets are more frequently resolved and isolated. On the other hand, we are resolving out some of the flux of extended features seen in the lower resolution 4.9 GHz image. As already noted, that means that the 8.5 GHz flux densities may be underestimated for large, extended sources and hence our calculated values of the 4.9–8.5 GHz spectral index are generally lower limits. On the other hand, the flux density determination for isolated, barely resolved cores and jets is more accurate and less influenced by background emission than is the case at 4.9 GHz.

At the two highest frequencies, because of the higher resolution, most of the extended structure seen at the two lower frequencies is resolved out and barely visible or not apparent (see Figure 2). As noted in Section 5.1, we convolve the 43 GHz images to produce a synthesized beam matching that at 22 GHz. Thus, we can fairly intercompare flux densities at the two higher frequencies, but it remains the case that spectral indices involving flux densities at either of the two lower frequencies will be lower limits.

6.3. SEDs of Cores and Other Pointlike or Barely Resolved Sources

The very different resolution of our images at different frequencies makes it difficult to compare flux densities directly, and hence to determine SEDs, especially for complex or resolved sources. We therefore elect to concentrate on unresolved or barely resolved sources or the obvious cores within more complex structure. These sources are flagged in Column (4) of Table 3 with a "C" indicating a well-defined core or "P" indicating an unresolved or barely resolved "pointlike" source. We are not claiming that these sources are necessarily unresolved at $\sim 1''$ scale, but rather that they are sufficiently isolated and regular in appearance that accurate flux densities can be obtained.

Of the 140 cluster sources for which the determination of an SED is possible, 73% or 52% are either pointlike or barely resolved in one or more of our three highest frequency images or have a clearly identifiable core at one or more of these same frequencies.

6.4. SEDs of Extended Sources

Because of the resolution effects discussed in Section 5.1, our SEDs and spectral indices for extended sources are less certain. In general, as expected (e.g., de Young 2002), the lobes and diffuse structure show steep spectral indices. In a few cases, as an experiment, we convolve the 8.5 GHz images to match the resolution of the 4.9 GHz images to allow direct comparison of fluxes. The results are shown in Table 4. From the table, it is clear that in these sample cases, at least, resolution is not

Table 3
Cluster Radio Sources

Name[a]	R.A. (J2000)	Decl. (J2000)	Type[b]	z[c]	f_L[d] (mJy)	f_C (mJy)	f_X (mJy)	f_K (mJy)	f_Q (mJy)	α_{CX}	α_{XK}	α_{KQ}	$f_{90,CX}$[e] (mJy)	$f_{90,KQ}$[f] (mJy)
0036−226B	9.7842	−22.3338	C	0.0654	129	74.33 ± 0.73	59.85 ± 0.43	39.12 ± 0.95	37.68 ± 1.16	−0.39	−0.44	−0.06	23.77	36.12
0037+209	9.9397	21.2256	−1	0.0622	143	10.43 ± 2.05	<0.66	<1.77	<1.49	< −4.97	...	...	...	...
0037+292	10.1180	29.5561	P/C	0.0716	12	6.20 ± 0.50	2.91 ± 0.32	2.55 ± 0.95	<1.43	−1.36	−0.14	< −0.88	0.12	...
0039+211	10.4230	21.4026	C	0.1030	670	101.70 ± 2.20	48.84 ± 0.55	24.70 ± 0.65	20.34 ± 0.80	−1.32	−0.70	−0.30	2.15	16.35
0039−095B	10.4603	−9.3031	C	0.0556	55	13.26 ± 0.64	7.04 ± 0.24	2.11 ± 0.48	<1.85	−1.14	−1.24	< −0.20	0.47	...
0039−095A	10.4509	−9.2840	−1	0.0556	48	20.98 ± 2.09	5.20 ± 0.90	<2.57	<1.48	−2.51	< −0.72	...	0.01	...
0039−097	10.4592	−9.4296	C	0.0556	82	...	6.86 ± 0.32	4.10 ± 0.48	3.95 ± 0.79	...	−0.53	−0.06	...	3.79
0043+201(1)	11.6233	20.4671	C	0.1053	563	19.63 ± 1.56	14.93 ± 0.50	<1.68	2.20 ± 0.76	−0.49	< −2.24	...	4.65	...
0043+201(2)	11.6222	20.4681	C	0.1053	563	19.63 ± 1.56	14.93 ± 0.50	10.63 ± 0.48	8.48 ± 0.65	−0.49	−0.35	−0.35	4.65	6.58
0046+011	12.1665	1.4302	C	0.0632	68	25.57 ± 0.88	5.76 ± 0.46	2.63 ± 0.57	3.19 ± 0.98	−2.68	−0.80	0.29	0.01	3.96
0047+241	12.4245	24.4451	C	0.0818	200	25.23 ± 1.08	16.68 ± 0.41	7.01 ± 0.53	7.52 ± 1.07	−0.75	−0.89	0.11	2.86	8.14
0047+242A(1)	12.4365	24.5003	−1	0.0818	24	11.86 ± 1.29	5.62 ± 0.57	1.03 ± 0.45	<2.12	−1.35	−1.74	< 1.10	0.23	...
0047+242A(2)	12.4348	24.5008	C	0.0818	24	11.86 ± 1.29	4.82 ± 0.49	1.89 ± 0.54	<2.12	−1.62	−0.96	< 0.18	0.20	...
0050−220(1)	13.3629	−21.7503	−1	0.0587	97	11.80 ± 1.36	6.78 ± 0.55	...	...	−1.00	...	...	0.64	...
0050−220(2)	13.3567	−21.7366	−1	0.0587	97	25.57 ± 0.89	13.94 ± 0.51	6.73 ± 0.71	3.21 ± 0.76	−1.09	−0.75	−1.13	1.05	1.40
0053+261A(1)	13.9624	26.4065	−1	0.1971	1327	82.20 ± 1.79	21.74 ± 0.68	<2.40	<2.21	−2.40	< −2.26	...	0.08	...
0053+261A(2)	13.9580	26.4131	−1	0.1971	1327	81.37 ± 2.06	24.13 ± 0.95	<2.06	<2.21	−2.19	< −2.52	...	0.14	...
0053−102B	13.9668	−9.9847	−1	0.0534	28	<1.95	<0.45	<2.40	<1.85	...	...	...	...	...
0053−015	14.1068	−1.2623	C	0.0444	1764	104.00 ± 4.30	44.33 ± 1.16	19.94 ± 1.15	18.98 ± 0.75	−1.54	−0.82	−0.08	1.17	17.96
0053−016	14.0074	−1.3430	−1	0.0444	1095	282.00 ± 8.00	106.53 ± −1.00	7.77 ± 1.74	<1.62	−1.75	−2.69	< −2.40	1.68	...
0100−221A	15.6880	−21.9041	P	0.0566	138	6.11 ± 0.57	4.50 ± 0.52	<3.22	...	−0.55	< −0.34	...	1.22	...
0108+173	17.7649	17.6521	P	0.0638	12	6.44 ± 0.61	3.51 ± 0.28	<1.96	<1.90	−1.09	< −0.60	...	0.26	...
0110+152	18.2483	15.4913	C	0.0444	719	31.50 ± 0.60	14.53 ± 2.84	4.97 ± 0.65	6.33 ± 0.60	−1.39	−1.10	0.37	0.54	8.30
0119+193(1)	20.5867	19.5881	P	0.0544	20	11.88 ± 0.61	8.79 ± 0.32	5.25 ± 0.46	2.40 ± 0.54	−0.54	−0.53	−1.20	2.43	0.99
0122+084	21.2819	8.6994	P	0.0498	51	4.03 ± 0.61	3.32 ± 0.32	1.24 ± 0.57	2.42 ± 0.47	−0.35	−1.01	1.02	1.45	5.13
0123−016A	21.4345	−1.3795	C	0.0180	910	77.60 ± 11.50	20.02 ± 1.67	10.93 ± −1.00	6.84 ± 0.57	−2.44	−0.62	−0.72	0.06	4.04
0123−016B	21.5027	−1.3451	P	0.0180	3270	107.53 ± 9.16	128.70 ± 3.61	121.70 ± 1.40	128.38 ± 1.00	0.32	−0.06	0.08	276.79	136.33
0124+189	21.7266	19.2145	C	0.0420	1345	310.00 ± 4.26	75.44 ± 1.91	24.98 ± 1.23	24.75 ± 0.96	−2.55	−1.13	−0.01	0.18	24.49
0139+073A	25.4977	7.6806	P	0.0616	43	6.27 ± 1.04	4.90 ± 0.23	2.07 ± 0.64	2.74 ± 0.81	−0.44	−0.88	0.43	1.71	3.76
0139+073B(2)	25.5183	7.6506	−1	0.0616	27	9.67 ± 1.84	3.28 ± 0.38	2.23 ± 0.84	<1.51	−1.95	−0.40	< −0.60	0.03	...
0149+359(1)	28.1932	36.1518	−1	0.0163	81	22.42 ± 1.09	10.78 ± 0.47	5.64 ± 0.88	5.40 ± 0.64	−1.32	−0.66	−0.07	0.48	5.14
0149+359(2)	28.1650	36.1714	P	0.0163	81	5.98 ± 1.36	5.51 ± 0.55	...	...	−0.15	...	...	3.89	...
0154+320(1)	29.3257	32.2400	−1	0.0894	372	91.00 ± 2.00	40.37 ± 1.40	<6.40	<1.67	−1.46	< −1.89	...	1.26	...
0154+320(2)	29.3175	32.2465	C	0.0894	372	91.00 ± 2.00	16.98 ± 0.92	3.15 ± 1.08	<1.59	−3.02	−1.73	< −1.04	0.53	...
0304−122(1)	46.7230	−12.1091	−1	0.0788	501	86.06 ± 2.70	40.07 ± 1.89	12.73 ± 2.30	2.35 ± 1.08	−1.38	−1.18	−2.58	1.54	0.35
0304−122(2)	46.7184	−12.1057	−1	0.0788	501	87.75 ± 2.00	45.55 ± 1.53	11.67 ± 1.40	6.56 ± 1.35	−1.18	−1.40	−0.88	2.79	3.43
0304−122(3)	46.7193	−12.1061	C	0.0788	501	87.75 ± 2.00	45.55 ± 1.53	4.93 ± 1.44	2.93 ± 0.86	−1.18	−2.28	−0.80	2.79	1.63
0306−237	47.0678	−23.5638	−1	0.0665	117	55.70 ± 1.20	33.71 ± 0.51	16.80 ± 0.59	14.15 ± 1.06	−0.90	−0.71	−0.26	3.97	11.67
0431−134(1)	68.5434	−13.3701	−1	0.0327	1160	106.00 ± 3.50	33.06 ± 0.98	23.10 ± 0.73	16.96 ± 0.74	−2.10	−0.37	−0.47	0.23	11.98
0445−205	72.0125	−20.4440	P	0.0734	95	15.50 ± 2.00	4.29 ± 0.52	2.30 ± 0.80	<1.97	−2.31	−0.64	< −0.24	0.02	...
0446−205	72.0431	−20.4160	C	0.0734	119	46.90 ± 1.60	17.37 ± 0.52	10.24 ± 0.63	8.58 ± 0.97	−1.79	−0.54	−0.27	0.25	7.03
0717+559	110.3399	55.8091	−1	0.0381	16	7.16 ± 1.17	2.29 ± 0.64	<2.12	<1.46	−2.05	< −0.08	...	0.02	...
0810+665	123.7207	66.4476	−1	0.1380	266	79.90 ± 1.50	38.21 ± 0.66	9.18 ± 1.30	6.17 ± 0.99	−1.33	−1.46	−0.61	1.65	3.95
0816+526(1)	124.9492	52.5368	−1	0.1890	2020	281.00 ± 2.30	140.29 ± 2.33	48.30 ± 4.32	19.62 ± 1.80	−1.25	−1.09	−1.38	7.27	7.12

Table 3
(Continued)

Name[a]	R.A. (J2000)	Decl. (J2000)	Type[b]	z[c]	f_L[d] (mJy)	f_C (mJy)	f_X (mJy)	f_K (mJy)	f_Q (mJy)	α_{CX}	α_{XK}	α_{KQ}	$f_{90,CX}$[e] (mJy)	$f_{90,KQ}$[f] (mJy)
0816+526(2)	124.9480	52.5408	C	0.1890	2020	. . .	145.40 ± 4.38	23.90 ± 6.30	3.59 ± 1.07	. . .	−1.85	−2.90	. . .	0.43
0816+526(3)	124.9471	52.5450	−1	0.1890	2020	497.10 ± 2.80	260.00 ± 3.00	59.24 ± 4.12	35.33 ± 2.40	−1.17	−1.52	−0.79	16.43	19.75
0836+290	129.8160	28.8441	P	0.0788	1022	156.00 ± 2.34	153.60 ± 0.91	117.06 ± 1.25	95.22 ± 1.18	−0.03	−0.28	−0.32	143.78	75.48
0909+162(1)	138.1463	15.9998	C	0.0851	183	25.00 ± 2.00	11.57 ± 1.45	2.94 ± 0.83	1.43 ± 0.64	−1.39	−1.41	−1.10	0.43	0.64
0909+162(2)	138.1408	15.9958	−1	0.0851	183	34.75 ± 1.35	18.25 ± 1.10	<2.50	<1.89	−1.16	< −2.04	. . .	1.17	. . .
0909+161	138.1274	15.9244	P	0.0851	23	16.41 ± 0.91	10.43 ± 0.34	6.56 ± 0.57	7.56 ± 0.63	−0.82	−0.48	0.22	1.51	8.87
1058+107	165.2392	10.5055	P	0.0360	24	9.96 ± 0.39	7.93 ± 0.29	4.85 ± 0.68	4.22 ± 0.74	−0.41	−0.50	−0.21	3.02	3.61
1108+289A	167.6990	28.6601	C	0.0321	34	9.50 ± 1.30	3.94 ± 0.72	2.55 ± 0.57	2.59 ± 1.01	−1.59	−0.45	0.02	0.09	2.63
1108+411(1)	167.9145	40.8380	−1	0.0794	771	235.00 ± 2.00	67.54 ± 1.21	16.30 ± 2.17	8.59 ± 2.57	−2.25	−1.46	−0.98	0.33	4.18
1108+411(2)	167.9144	40.8406	C	0.0794	771	235.00 ± 2.00	37.70 ± 0.82	13.37 ± 1.65	3.76 ± 1.03	−3.30	−1.06	−1.94	0.19	0.90
1108+411(3)	167.9120	40.8391	C	0.0794	771	235.00 ± 2.00	71.01 ± 1.46	10.37 ± 2.17	. . .	−2.16	−1.97	. . .	0.35	. . .
1108+410A	167.9184	40.7853	−1	0.0794	116	<4.35	<1.21	<2.37	<1.46	. . .	. . .	. . .	. . .	. . .
1108+410B	167.9319	40.8210	P	0.0794	23	6.99 ± 1.08	5.27 ± 0.79	<2.44	<1.49	−0.51	< −0.79	. . .	1.59	. . .
1113+295B(1)	169.1192	29.2860	−1	0.0471	22	15.92 ± 4.15	<4.86	4.14 ± 1.05	2.16 ± 0.66	< −2.14	. . .	−1.00	. . .	1.04
1113+295B(2)	169.0945	29.2523	P	0.0471	22	54.08 ± 4.67	31.78 ± 4.06	. . .	. . .	−0.96	. . .	. . .	3.30	. . .
1113+295C	169.1438	29.2547	C	0.0471	1888	289.90 ± 6.10	97.35 ± 2.90	35.72 ± 1.95	37.28 ± 1.07	−1.97	−1.03	0.07	0.93	39.12
1129+562	173.0960	55.9678	−1	0.0531	39	8.22 ± 0.49	2.60 ± 0.59	<2.00	<2.33	−2.07	< −0.27	. . .	0.02	. . .
1130+148	173.2561	14.5346	C	0.0834	167	13.68 ± 0.41	8.82 ± 0.39	3.42 ± 0.76	3.56 ± 1.08	−0.79	−0.97	0.06	1.36	3.73
1130−037	173.2713	−4.0133	P	0.0484	791	158.51 ± 2.10	107.40 ± 1.37	62.13 ± 0.86	. . .	−0.70	−0.56	. . .	20.45	. . .
1131+493	173.4967	49.0622	C	0.0338	835	131.25 ± 2.00	91.44 ± 1.32	52.85 ± 1.10	41.84 ± 0.92	−0.65	−0.56	−0.36	19.60	32.17
1132+492	173.6940	48.9562	C	0.0338	475	30.38 ± 0.83	31.86 ± 0.74	26.76 ± 0.88	18.59 ± 0.86	0.09	−0.18	−0.56	39.02	12.34
1132+493	173.7056	49.0779	P	0.0338	31	12.61 ± 0.49	7.15 ± 0.43	<2.45	1.81 ± 0.83	−1.02	< −1.10	. . .	0.64	. . .
1141+466(1)	175.9146	46.3549	P	0.1162	814	149.40 ± 0.50	44.90 ± 0.66	3.47 ± 1.04	1.31 ± 0.73	−2.17	−2.63	−1.49	0.27	0.44
1141+466(2)	175.9158	46.3564	C	0.1162	814	149.40 ± 0.50	66.15 ± 0.62	11.35 ± 1.40	0.95 ± 0.56	−1.47	−1.81	−3.79	0.39	0.06
1141+676	176.1526	67.4060	P	0.1164	196	68.94 ± 0.47	37.75 ± 0.51	16.84 ± 1.20	10.48 ± 0.95	−1.08	−0.83	−0.72	2.90	6.15
1142+198	176.2709	19.6064	C	0.0214	5450	723.75 ± 9.55	432.27 ± 4.22	215.48 ± 2.70	172.11 ± 2.30	−0.93	−0.71	−0.34	48.08	133.66
1153+736	178.9965	73.4154	P	0.0836	64	27.66 ± 0.59	19.33 ± 0.75	3.01 ± 1.09	3.96 ± 1.74	−0.65	−1.91	0.42	4.20	5.39
1155+266	179.5839	26.3533	C	0.1120	880	13.80 ± 6.70	1.63 ± 0.73	6.92 ± 0.93	7.09 ± 0.64	−3.85	1.48	0.04	0.00	7.29
1159+583(1)	180.5143	58.0337	−1	0.1035	765	110.00 ± 1.00	53.15 ± 0.88	19.66 ± 2.33	8.70 ± 1.70	−1.31	−1.02	−1.25	2.40	3.48
1159+583(3)	180.5203	58.0373	−1	0.1035	765	124.00 ± 1.10	54.62 ± 0.86	23.74 ± 3.00	12.50 ± 2.10	−1.48	−0.85	−0.98	1.66	6.07
1201+282	180.9028	27.9443	C	0.1390	215	2.93 ± 0.31	1.87 ± 0.43	4.94 ± 0.86	1.69 ± 0.74	−0.81	1.00	−1.64	0.28	0.51
1201+026(1)	181.0303	2.4099	C	0.0844	244	120.00 ± 1.00	29.82 ± 1.32	3.75 ± 1.50	. . .	−2.51	−2.13	. . .	0.26	. . .
1201+026(2)	181.0264	2.4118	C	0.0844	244	120.00 ± 1.00	39.40 ± 1.40	8.11 ± 0.96	6.06 ± 0.90	−2.01	−1.62	−0.45	0.34	4.37
1201+026(3)	181.2723	2.4135	C	0.0844	244	120.00 ± 1.00	25.65 ± 1.06	. . .	. . .	−2.78	. . .	. . .	0.22	. . .
1207+722	182.5808	71.9993	C	0.1226	256	. . .	47.53 ± 2.40	6.56 ± 2.09	<2.58	. . .	−2.03	< −1.43	. . .	. . .
1221+615(1)	185.8762	61.2473	−1	0.2308	321	69.15 ± 0.57	34.34 ± 0.89	12.50 ± 1.49	3.89 ± 1.35	−1.26	−1.04	−1.78	1.74	1.05
1221+615(2)	185.8740	61.2521	−1	0.2308	321	49.46 ± 0.54	24.78 ± 0.69	5.98 ± 1.55	<2.58	−1.24	−1.46	< −1.28	1.30	. . .
1224+091	186.8264	8.8431	C	0.0896	48	<3.40	5.05 ± 0.68	<2.39	<2.91	. . .	< −0.77	. . .	. . .	. . .
1225+636(1)	186.9687	63.3840	−1	0.1459	210	70.32 ± 0.82	19.53 ± 0.65	11.80 ± 4.80	<1.66	−2.31	−0.52	< −3.00	0.08	. . .
1225+636(2)	186.9634	63.3848	C	0.1459	210	70.32 ± 0.82	22.41 ± 0.63	5.04 ± 1.27	5.47 ± 1.00	−2.06	−1.53	0.13	0.10	6.00
1231+674	188.3085	67.1289	C	0.1071	879	18.00 ± 1.00	11.00 ± 1.33	7.33 ± 1.23	4.43 ± 0.84	−0.89	−0.42	−0.77	1.35	2.51
1232+414(1)	188.6250	41.1599	C	0.1908	689	<17.00	19.51 ± 2.40	<2.67	<1.39	. . .	< −2.04	. . .	. . .	. . .
1232+414(2)	188.6142	41.1668	−1	0.1908	689	105.30 ± 1.50	48.94 ± 0.71	19.85 ± 2.50	12.67 ± 1.35	−1.38	−0.93	−0.69	1.87	7.65
1233+169	189.0338	16.6414	P	0.0784	630	189.00 ± 2.50	64.22 ± 1.16	33.21 ± 0.99	20.39 ± 0.96	−1.94	−0.68	−0.75	0.65	11.78

Table 3
(Continued)

Name[a]	R.A. (J2000)	Decl. (J2000)	Type[b]	z[c]	f_L[d] (mJy)	f_C (mJy)	f_X (mJy)	f_K (mJy)	f_Q (mJy)	α_{CX}	α_{XK}	α_{KQ}	$f_{90,CX}$[e] (mJy)	$f_{90,KQ}$[f] (mJy)
1233+168	189.1079	16.5384	C	0.0784	1338	65.00 ± 12.00	11.13 ± 2.40	4.62 ± 1.17	3.28 ± 0.90	−3.18	−0.90	−0.52	0.01	2.23
1238+188	190.2511	18.5537	C	0.0718	537	48.35 ± 1.41	18.32 ± 0.80	5.77 ± 1.03	4.75 ± 0.91	−1.75	−1.19	−0.30	0.29	3.82
1243+699	191.4726	69.6582	C	0.2307	220	38.76 ± 1.39	6.66 ± 0.60	4.27 ± 1.26	0.80 ± 0.43	−3.17	−0.46	−2.56	0.00	0.12
1256+281	194.8462	27.9112	C	0.0231	450	59.69 ± 1.39	37.62 ± 1.53	<2.56	<1.85	−0.83	< −2.76	...	5.26	...
1257+282(1)	194.8964	27.9579	−1	0.0231	215	39.83 ± 0.89	22.64 ± 0.45	7.83 ± 1.94	3.00 ± −1.00	−1.02	−1.09	−1.47	2.04	1.02
1257+282(2)	194.9002	27.9610	−1	0.0231	215	50.20 ± 1.00	23.19 ± 0.47	7.54 ± 1.18	2.82 ± 0.71	−1.39	−1.15	−1.50	0.86	0.93
1301+195	195.9442	19.2715	P	0.0649	74	22.51 ± 0.28	13.70 ± 0.27	6.20 ± 0.75	1.96 ± 0.55	−0.89	−0.81	−1.76	1.65	0.54
1300+677	195.6686	67.4780	−1	0.1055	298	137.20 ± 0.60	87.48 ± 0.77	15.90 ± 0.90	<3.00	−0.81	−1.75	< −2.55	12.86	...
1320+584(1)	200.7321	58.1675	−1	0.1932	325	78.62 ± 1.02	50.00 ± 1.00	13.94 ± 1.33	...	−0.82	−1.31	...	7.27	...
1320+584(2)	200.7268	58.1711	C	0.1932	325	53.21 ± 0.81	27.87 ± 0.67	<2.85	...	−1.16	< −2.34	...	1.77	...
1333+412(1)	203.8350	40.9999	−1	0.2290	797	169.70 ± 0.90	63.05 ± 0.62	22.77 ± 1.40	...	−1.78	−1.04	...	0.93	...
1333+412(2)	203.8320	41.0024	−1	0.2290	797	161.30 ± 0.90	62.34 ± 0.64	18.44 ± 1.21	...	−1.71	−1.25	...	1.09	...
1339+266A	205.4552	26.3738	−1	0.0724	40	15.90 ± 0.64	6.39 ± 0.67	<1.63	<1.59	−1.64	< −1.40	...	0.13	...
1339+266B	205.4606	26.3715	−1	0.0724	287	91.95 ± 0.61	41.04 ± 0.64	1.87 ± −1.00	<1.59	−1.45	−3.17	< −0.25	1.32	...
1346+268A	207.2186	26.5928	P	0.0622	883	234.60 ± 0.50	110.74 ± 0.84	21.79 ± 1.02	12.24 ± 0.67	−1.35	−1.67	−0.88	4.52	6.40
1346+268B	207.2474	26.5594	−1	0.0622	35	10.75 ± 0.67	12.05 ± 1.17	4.14 ± 0.96	<1.50	0.21	−1.10	< −1.55	19.60	...
1415+084(1)	214.3803	8.2084	C	0.0570	331	29.83 ± 1.66	8.27 ± 0.72	3.60 ± 0.59	...	−2.31	−0.85	...	0.03	...
1415+084(2)	214.3826	8.2101	C	0.0570	331	29.83 ± 1.66	5.88 ± 0.82	<0.78	...	−2.93	< −2.07	...	0.02	...
1418+253(1)	215.1731	25.1499	−1	0.0780	116	22.27 ± 0.51	9.45 ± 0.75	1.28 ± 0.50	1.70 ± 0.71	−1.54	−2.05	0.43	0.24	2.34
1418+253(2)	215.1747	25.1461	−1	0.0780	116	<26.70	6.63 ± 0.76	2.03 ± 0.66	3.76 ± 0.84	...	−1.21	0.94	...	7.53
1418+253(3)	215.1758	25.1438	C	0.0780	116	<26.70	6.65 ± 0.79	2.15 ± 0.80	<1.56	−2.93	−1.16	< −0.49	...	...
1418+253(4)	215.1767	25.1408	−1	0.0780	116	21.03 ± 0.59	6.36 ± 0.65	<1.74	<1.84	−2.15	< −1.33	...	0.04	...
1424+169(1)	216.6422	16.7507	−1	0.0528	97	9.55 ± 0.58	8.20 ± 0.73	...	...	−0.27	...	...	4.28	...
1424+169(2)	216.6313	16.7633	−1	0.0528	97	7.94 ± 0.70	1.92 ± 0.63	...	...	−2.56	...	...	0.00	...
1424+167(1)	216.8221	16.5548	−1	0.0528	103	11.93 ± 0.57	7.15 ± 0.44	4.75 ± 1.32	...	−0.92	−0.42	...	0.81	...
1435+249(1)	219.3126	24.7591	C	0.0883	175	11.80 ± 0.56	9.21 ± 0.39	7.72 ± 0.61	5.77 ± 0.58	−0.45	−0.18	−0.45	3.20	4.16
1435+249(2)	219.3168	24.7653	−1	0.0883	175	11.69 ± 0.88	5.54 ± 0.71	<1.98	...	−1.35	< −1.06	...	0.23	...
1435+250	219.3200	24.8693	C	0.0883	206	23.03 ± 0.73	12.22 ± 0.45	6.53 ± 1.10	4.62 ± 0.83	−1.14	−0.64	−0.53	0.82	3.12
1433+553	218.8688	55.1311	C	0.1396	447	73.92 ± 1.02	16.81 ± 0.55	7.95 ± 0.83	...	−2.67	−0.77	...	0.03	...
1435+038(0)	219.5993	3.6729	C	0.2240	801	103.16 ± 0.78	11.25 ± 0.85	<16.06	...	−3.99	< 0.37	...	0.41	...
1435+038(1)	219.5946	3.6713	−1	0.2240	801	103.16 ± 0.78	47.29 ± 0.54	12.21 ± 2.13	...	−1.40	−1.39	...	1.70	...
1435+038(2)	219.5886	3.6702	−1	0.2240	801	114.12 ± 0.73	55.45 ± 0.51	15.91 ± 1.61	...	−1.30	−1.28	...	2.56	...
1435+038(4)	219.5960	3.6714	−1	0.2240	801	89.03 ± 1.37	<2.54	<2.93	...	< −6.41	...	...	...	...
1452+188	223.6312	18.6423	P	0.0579	38	11.99 ± 0.23	7.71 ± 0.25	2.11 ± 0.56	...	−0.80	−1.33	...	1.17	...
1508+059(1)	227.7339	5.7446	−1	0.0767	489	60.51 ± 0.46	21.31 ± 0.42	4.07 ± 1.03	...	−1.88	−1.70	...	0.25	...
1508+065(1)	227.8630	6.3472	−1	0.0817	552	127.65 ± 0.72	54.79 ± 0.66	18.02 ± −1.00	...	−1.52	−1.14	...	1.49	...
1508+065(2)	227.8584	6.3503	−1	0.0817	552	127.44 ± 0.70	56.48 ± 0.62	15.35 ± 2.17	...	−1.47	−1.34	...	1.76	...
1508+182(1)	227.7893	18.0300	−1	0.1163	346	74.34 ± 0.88	30.50 ± 0.65	<9.33	...	−1.60	< −1.22	...	0.68	...
1508+182(2)	227.7847	18.0326	−1	0.1163	346	68.61 ± 0.96	26.85 ± 0.61	6.90 ± 1.51	...	−1.69	−1.39	...	0.49	...
1510+076(1)	228.1405	7.4249	−1	0.0451	17	10.59 ± 1.54	2.76 ± 0.55	<2.87	...	−2.42	< 0.04	...	0.01	...
1510+076(2)	228.1427	7.4318	C	0.0451	17	10.59 ± 1.54	1.97 ± 0.45	1.57 ± 0.70	...	−3.03	−0.23	...	0.01	...
1514+072	229.1854	7.0216	P	0.0348	5390	897.61 ± 2.89	691.40 ± 2.70	393.16 ± 5.70	...	−0.47	−0.58	...	227.36	...
1520+087	230.7719	8.6094	−1	0.0355	13	5.59 ± 0.47	2.11 ± 0.37	<2.30	...	−1.75	< 0.09	...	0.03	...
1525+290	231.9350	28.9183	C	0.0656	224	88.69 ± 0.64	28.84 ± 0.78	5.70 ± 0.84	3.31 ± 0.90	−2.02	−1.66	−0.83	0.24	1.80

Table 3
(Continued)

Name[a]	R.A. (J2000)	Decl. (J2000)	Type[b]	z[c]	f_L[d] (mJy)	f_C (mJy)	f_X (mJy)	f_K (mJy)	f_Q (mJy)	α_{CX}	α_{XK}	α_{KQ}	$f_{90,CX}$[e] (mJy)	$f_{90,KQ}$[f] (mJy)
1530+282	233.1860	28.0631	C	0.0734	352	133.24 ± 1.03	14.71 ± 0.69	4.87 ± 0.82	1.99 ± 1.13	−3.97	−1.13	−1.37	0.00	0.73
1531+312(1)	233.3132	31.1285	−1	0.0670	49	6.89 ± 0.37	2.81 ± 0.32	<2.17	<1.61	−1.62	< −0.27	...	0.06	...
1531+312(2)	233.3137	31.1307	C	0.0670	49	6.89 ± 0.37	1.28 ± 0.32	<2.17	<2.80	−3.03	< 0.54	...	0.03	...
1531+312(3)	233.3169	31.1331	−1	0.0670	49	8.53 ± 0.38	4.39 ± 0.45	<2.17	<2.25	−1.20	< −0.72	...	0.26	...
1555+356(2)	239.4258	35.5076	−1	0.1579	216	57.62 ± 0.63	14.60 ± 0.41	7.02 ± 1.85	3.03 ± 0.90	−2.47	−0.75	−1.28	0.04	1.18
1555+356(3)	239.4267	35.5094	C	0.1579	216	23.70 ± 0.44	16.80 ± 0.44	5.38 ± 0.91	3.58 ± 1.04	−0.62	−1.17	−0.62	0.83	2.26
1556+274	239.5585	27.2723	−1	0.0896	130	30.38 ± 0.41	16.97 ± 0.36	7.97 ± 1.59	<1.92	−1.05	−0.77	< −2.18	1.42	...
1559+161(1)	240.5703	15.9745	−1	0.0354	17	6.83 ± 0.36	4.97 ± 0.42	<1.80	...	−0.57	< −1.04	...	1.28	...
1602+178B(1)	241.2872	17.7314	−1	0.0368	780	116.48 ± 1.62	76.02 ± 2.36	10.84 ± 1.27	...	−0.77	−2.00	...	12.34	...
1602+178B(1.5)	241.2875	17.7299	−1	0.0368	780	...	...	10.75 ± 1.26	...	...	...	...	...	...
1602+178B(2)	241.2880	17.7270	−1	0.0368	780	213.70 ± 1.75	139.80 ± 2.39	<4.73	...	−0.76	< −3.47	...	22.92	...
1603+165	241.3717	16.4357	C	0.0372	44	9.04 ± 0.35	4.78 ± 0.33	2.48 ± 0.69	...	−1.15	−0.67	...	0.32	...
1610+296(2)	243.1456	29.4814	C	0.0320	119	38.00 ± − 1.00	<0.59	2.83 ± 0.86	<1.66	< −7.50	...	< −0.82	...	...
1626+396	247.1594	39.5513	−1	0.0299	3480	440.00 ± − 1.00	185.00 ± − 1.00	...	...	−1.56	...	...	4.61	...
1638+468	250.0925	46.7131	−1	0.2070	212	74.10 ± 0.73	44.70 ± 0.84	...	...	−0.91	...	...	5.19	...
1657+325A	254.7545	32.4941	−1	0.0628	171	22.00 ± − 1.00	1.18 ± 0.30	<3.28	<1.82	−5.27	< 1.05	...	0.00	...
1657+325B	254.7852	32.5000	−1	0.0628	12	...	<0.62	<2.86	...	...	...	...	...	...
1707+344(1)	257.4131	34.4283	−1	0.0806	680	100.38 ± 0.81	56.81 ± 1.53	22.00 ± 3.20	13.90 ± − 1.00	−1.03	−0.97	−0.70	5.02	8.29
1707+344(2)	257.4096	34.4336	−1	0.0806	680	108.22 ± 0.74	62.07 ± 1.29	23.00 ± 2.50	7.00 ± 2.80	−1.00	−1.02	−1.82	5.81	1.84
1708+345	257.4972	34.5120	P	0.0806	16	9.53 ± 0.67	4.95 ± 0.81	3.83 ± 1.77	<2.19	−1.18	−0.26	< −0.85	0.30	...
1709+397B	257.7364	39.6926	C	0.0656	543	106.15 ± 0.70	60.28 ± 0.75	23.20 ± 2.50	12.13 ± 2.50	−1.02	−0.98	−0.99	5.41	5.85
1712+640	258.0974	64.0334	C	0.0808	290	82.50 ± 1.00	45.76 ± 1.15	4.67 ± 0.77	<1.77	−1.06	−2.34	< −1.48	3.71	...
1712+641(1)	258.2699	64.1157	−1	0.0808	66	26.93 ± 0.99	8.41 ± 0.80	3.59 ± 1.23	<1.87	−2.10	−0.87	< −1.00	0.06	...
1712+641(2)	258.2661	64.1177	C	0.0808	66	26.93 ± 0.99	8.80 ± 0.54	1.28 ± 0.41	<1.87	−2.01	−1.98	< 0.58	0.06	...
1713+641(1)	258.3701	64.0443	−1	0.0808	250	85.10 ± 0.66	37.21 ± 0.56	9.33 ± 1.44	4.84 ± 1.30	−1.49	−1.42	−1.00	1.10	2.31
1713+641(2)	258.3706	64.0457	C	0.0808	250	85.10 ± 0.66	48.83 ± 0.81	7.26 ± 0.79	5.02 ± 0.79	−1.00	−1.96	−0.56	1.44	3.31
1713+641(3)	258.3735	64.0503	−1	0.0808	250	70.30 ± 0.65	37.34 ± 0.67	4.26 ± 0.88	<1.86	−1.14	−2.23	< −1.27	2.52	...
1706+786	255.8676	78.6321	−1	0.0581	157	42.81 ± 0.69	23.50 ± 0.58	5.98 ± 1.11	<1.78	−1.08	−1.40	< −1.85	1.82	...
1705+786	255.7604	78.5992	−1	0.0581	62	26.00 ± − 1.00	6.91 ± 0.73	<2.30	<1.83	−2.39	< −1.13	...	0.02	...
1706+787	255.8668	78.6660	P	0.0581	39	5.06 ± 0.60	3.96 ± 0.53	<1.01	<1.99	−0.44	< −1.40	...	1.39	...
1703+787	255.2176	78.6901	−1	0.0581	10	2.14 ± 0.45	1.25 ± 0.36	<2.32	<3.48	−0.97	< 0.63	...	0.13	...
1820+689	274.9260	68.9476	C/P	0.0880	801	83.27 ± 1.61	52.65 ± 1.54	31.11 ± 1.12	24.36 ± 0.78	−0.83	−0.54	−0.37	7.47	18.50
1826+747(1)	276.2349	74.7308	−1	0.1271	244	38.53 ± 1.11	21.63 ± 0.71	1.44 ± 0.65	1.85 ± 0.65	−1.04	−2.78	0.38	1.85	2.46
1826+747(2)	276.2153	74.7316	−1	0.1271	244	44.98 ± 1.27	16.27 ± 0.54	3.68 ± 1.30	2.14 ± 0.76	−1.83	−1.53	−0.83	0.21	1.16
1849+702(1)	282.3256	70.3535	C	0.0899	163	18.83 ± 0.54	14.47 ± 0.34	8.28 ± 0.49	9.48 ± 0.65	−0.47	−0.57	0.21	4.71	11.04
1857+799	283.4678	80.0474	P	0.2139	180	2.80 ± 0.51	2.66 ± 0.27	5.34 ± 1.44	2.61 ± 0.60	−0.09	0.71	−1.09	2.15	1.17
2124−124(1)	321.7414	−12.2154	−1	0.1760	251	96.09 ± 1.10	38.45 ± 1.10	<2.43	<2.10	−1.65	< −2.83	...	0.78	...
2124−124(2)	321.7384	−12.2144	C	0.1760	251	96.09 ± 1.10	26.53 ± 0.58	8.96 ± 1.13	8.38 ± 0.81	−2.32	−1.11	−0.10	0.54	7.77
2142−202	326.3143	−19.9952	−1	0.0576	351	2.45 ± 1.27	<0.70	2.28 ± 1.06	<1.74	< −2.26	...	< −0.41	...	...
2149−158C(1)	327.9990	−15.6384	C	0.0646	176	29.88 ± 1.80	12.76 ± 1.03	5.24 ± 1.07	1.83 ± 0.75	−1.53	−0.91	−1.61	0.34	0.56
2149−158C(2)	327.9796	−15.6263	−1	0.0646	176	64.00 ± 3.40	14.67 ± 1.70	<2.93	...	−2.65	< −1.65	...	0.03	...

Table 3
(Continued)

Name[a]	R.A. (J2000)	Decl. (J2000)	Type[b]	z[c]	f_L[d] (mJy)	f_C (mJy)	f_X (mJy)	f_K (mJy)	f_Q (mJy)	α_{CX}	α_{XK}	α_{KQ}	$f_{90,CX}$[e] (mJy)	$f_{90,KQ}$[f] (mJy)
2154−080A(1)	329.2532	−7.8474	−1	0.0584	460	81.60 ± 1.14	51.47 ± 2.65	36.00 ± −1.00	. . .	−0.83	−0.37	. . .	7.22	. . .
2154−080A(2)	329.2569	−7.8398	C	0.0584	460	81.20 ± 1.13	11.11 ± 1.05	5.45 ± 0.53	4.04 ± 0.71	−3.58	−0.73	−0.46	0.00	2.88
2154−080A(3)	329.2635	−7.8362	−1	0.0584	460	73.43 ± 1.06	46.53 ± 2.41	18.00 ± −1.00	. . .	−0.82	−0.97	. . .	6.66	. . .
2154−080B	329.3896	−7.7943	C	0.0584	430	92.43 ± 1.16	13.88 ± 0.71	6.47 ± 0.92	5.67 ± 0.96	−3.42	−0.78	−0.20	0.00	4.89
2228−087	337.8701	−8.4849	P	0.0810	107	10.89 ± 0.67	10.48 ± 0.31	6.39 ± 0.72	6.30 ± 0.62	−0.07	−0.51	−0.02	8.89	6.20
2229−086	337.9302	−8.4088	C	0.0810	812	64.79 ± 2.52	33.38 ± 1.13	20.42 ± 0.85	16.84 ± 0.70	−1.19	−0.50	−0.29	1.98	13.56
2247+106B	342.5818	10.9034	−1	0.0768	14	2.44 ± 0.24	0.99 ± 0.28	3.07 ± 1.08	<1.11	−1.62	1.16	< −1.55	0.02	. . .
2321+164	350.9762	16.6804	−1	0.0416	46	20.40 ± 0.57	9.95 ± 0.44	6.96 ± 0.10	2.30 ± −1.00	−1.29	−0.37	−1.69	0.47	0.66
2322+143A(1)	351.1339	14.6396	C	0.0421	187	65.59 ± 1.36	24.47 ± 0.80	6.75 ± 0.92	4.94 ± 0.78	−1.78	−1.32	−0.48	0.37	3.47
2322+143B(1)	351.1548	14.6425	C	0.0421	76	25.85 ± 0.95	14.01 ± 0.54	6.84 ± 1.05	3.15 ± 0.71	−1.10	−0.74	−1.18	1.03	1.32
2322−123	351.3324	−12.1241	P	0.0852	1699	415.59 ± 0.91	205.83 ± 0.66	59.58 ± 1.22	31.26 ± 0.99	−1.27	−1.27	−0.99	10.31	15.13
2332+270(2)	353.7570	27.3714	−1	0.0617	61	9.23 ± 0.45	<1.02	<1.47	<1.90	< −3.97	. . .	. . .	. . .	. . .
2333+208(1)	354.1270	21.1466	P	0.0569	55	11.41 ± 0.33	6.60 ± 0.27	4.30 ± 0.62	4.25 ± 0.74	−0.99	−0.44	−0.02	0.64	4.19
2333+208(3)	354.1654	21.1021	P	0.0569	55	2.33 ± 0.51	. . .	. . .	. . .	. . .	. . .	. . .	. . .	. . .
2335+267(1)	354.6225	27.0314	C	0.0321	7650	267.48 ± 15.60	212.63 ± 5.08	139.12 ± 2.16	102.95 ± 1.33	−0.41	−0.44	−0.46	79.97	73.37
2335+267(2)	354.6330	27.0244	−1	0.0321	7650	316.87 ± 22.30	184.23 ± 12.60	<109.90	. . .	−0.98	< −0.53	. . .	18.27	. . .
2348+058	357.7107	6.1495	P	0.0556	50	8.49 ± 0.29	3.02 ± 0.24	5.28 ± 1.88	<1.77	−1.86	0.57	< −1.67	0.04	. . .
2352+261(1)	358.8519	26.4047	C	0.2404	311	3.89 ± 0.84	1.48 ± 0.57	1.91 ± 0.82	<3.25	−1.74	0.26	< 0.81	0.02	. . .
2352+261(3)	358.8247	26.4162	−1	0.2404	311	28.44 ± 1.58	12.30 ± 0.85	. . .	. . .	−1.51	. . .	. . .	0.35	. . .

Notes.

[a] Source name from Owen & Ledlow (1997), which is based on B1950 positions; parentheses denote multiple components.

[b] Morphology of the sources: "−1" denotes extended source; "C" means core; "P" refers to pointlike.

[c] Redshift taken from Owen & Ledlow (1997).

[d] 1.4 GHz flux from Owen & Ledlow (1997).

[e] Predicted flux at 90 GHz based on the fluxes at C and X bands and α_{CX}.

[f] Predicted flux at 90 GHz based on the fluxes at K and Q bands and α_{KQ}.
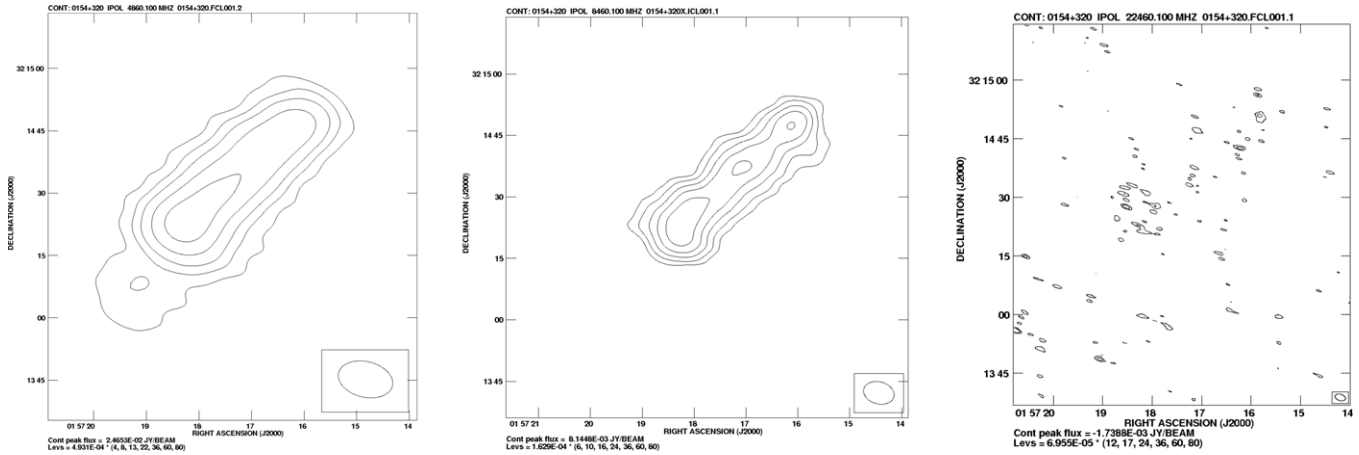
Figure 1. Left to right: a source (0154+320) imaged at C, X, and K bands, showing the loss of flux due to resolution; beam profiles at each frequency are shown in the small box on the lower right of each panel. Contours are selected to reveal the main source properties.
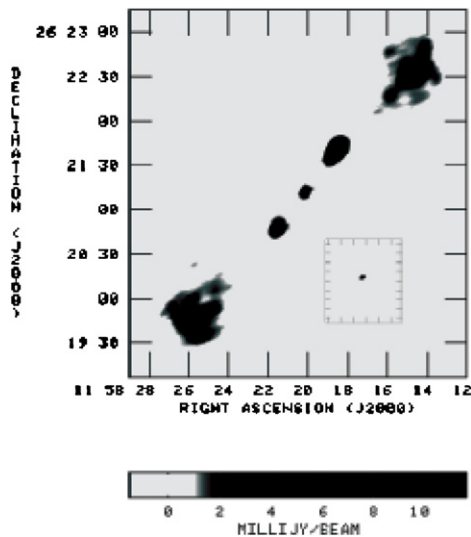
Figure 2. Main figure: the source 1155+266 imaged at 8.5 GHz. Insert (to same scale): the same source at 22 GHz, showing no evidence of emission from the lobes; the core remains.

significantly affecting the 8.5 GHz fluxes in major ways, except for clearly resolved sources.

If only emission from lobes and extended structure were involved, the generally steep spectra would ensure that most cluster radio sources would present minimal problems for SZE measurements carried out at frequencies above, say, 90 GHz. The second-to-last column of Table 3 lists estimated 90 GHz flux densities based on the X-band flux, assuming that the spectral index between 4.9 and 8.5 GHz can be directly extrapolated to 90 GHz. The last column of the table is the estimate based on the Q-band flux where available, using the spectral index between 22 and 43 GHz. Note the frequent substantial differences in extrapolated flux.

6.5. SEDs of Cores

However, we find that the cores and other unresolved or barely resolved structures generally have flatter spectra, and in particular that many sources exhibit a substantial change in spectral index at frequencies above 22 GHz. This means that cluster radio sources may present a larger problem for sensitive SZE measurements than might be expected from the extrapolation of low-frequency measurements (e.g., LM07). For

that reason, as well as because of the difficulty of obtaining the fluxes of extended sources, we concentrate on cores and other unresolved or barely resolved components. We will focus on the 73 sources that are detected in three or more bands with these morphologies. It is important to recall, however, that even for these relatively compact and uncomplicated sources, resolution effects may cause us to miss some of the flux. Since we use tapered Q-band flux densities, α_{KQ} is nominally unaffected, but resolution may affect the spectral indices at lower frequencies.

An efficient way to quantify the distribution of the spectral shapes is through the "two-color" plot (Sadler et al. 2006), as shown in Figure 3, where the spectral index between the C and X bands (α_{CX}) is plotted for 57 core/pointlike sources against that between the K and Q bands (α_{KQ}). Throughout our analysis, we adopt the notation for the spectral index such that a power-law spectrum is described as $S_\nu \propto \nu^\alpha$. Following the common practice of referring to sources with $\alpha < -0.5$ as "steep," and "flat/inverted" otherwise, the α_{CX}–α_{KQ} space is divided into four quadrants, as delineated by the two dashed lines in Figure 3. Starting from the first quadrant (upper-right corner) and going counterclockwise, the quadrants contain sources with flat/inverted spectra, with spectra that turn flat above 8 GHz, with steep spectra, and with spectra that peak around 10 or so GHz (which we refer to as "approximately gigahertz peaked spectrum" ($\approx$GPS) sources), respectively. The relative proportions of these types of spectral shape are shown in Figure 3. We can also see that $\sim$84% show a more positive high-frequency spectral index than low-frequency spectral index, that is a flattening at frequencies above 8 GHz or so. Only about one-third of the sources have steep spectra from 4.9 to 43 GHz. The lack of correlations of the data points clearly suggests that the spectral shape of the core/pointlike sources is nontrivial.

If we include all 75 sources irrespective of their morphology, the relative proportions of the four quadrants become 13.1% (flat/inverted), 35.7% (upturn), 48.8% (steep), and 2.4% ($\approx$GPS).

With $\sim$100 sources detected at 18 GHz with the Australian Telescope Compact Array (ATCA), Sadler et al. (2006) study the distribution of the spectral shapes with the two-color plot, where their low- and high-frequency indices are based on 0.8 and 5 GHz, and 8 and 18 GHz fluxes, respectively. We note that they separate the flat/inverted sources from steep ones at $\alpha = 0$; adopting the same definition, we find that the great majority of our sources become steep (73%) and upturn (23%). This seems to suggest that our cluster sources exhibit steeper spectra than

Table 4
Effect of Tapering on *X*-Band Flux Measurements

Source	Extended	*X* Flux (Untapered) (mJy)	*X* Flux (Tapered) (mJy)	*C* Flux (mJy)	α_{CX} (Tapered)
0036−226B		59.850 ± 0.430	61.770 ± 0.520	74.330 ± 0.733	−0.334
0037+292		2.910 ± 0.320	3.110 ± 0.340	6.200 ± 0.500	−1.245
0039−095B		7.040 ± 0.240	7.230 ± 0.290	13.260 ± 0.644	−1.094
0100−221A		4.495 ± 0.520	3.180 ± 0.260	6.110 ± 0.570	−1.178
0119+193(1)		8.785 ± 0.320	8.480 ± 0.300	11.880 ± 0.610	−0.608
0124+189	Yes	75.440 ± 1.910	132.900 ± 2.830	310.000 ± 4.260	−1.528
0139+073A		4.898 ± 0.230	4.710 ± 0.320	6.270 ± 1.040	−0.516
0909+161		10.430 ± 0.340	11.380 ± 0.410	16.410 ± 0.910	−0.660
1058+107		7.935 ± 0.290	9.920 ± 0.480	9.957 ± 0.390	−0.007
1130+148		8.820 ± 0.390	9.630 ± 0.560	13.680 ± 0.410	−0.633
1132+492		31.860 ± 0.740	34.640 ± 0.900	30.380 ± 0.830	0.237
1201+282		1.870 ± 0.430	1.680 ± 0.550	2.930 ± 0.310	−1.003
1301+195		13.700 ± 0.270	12.790 ± 0.290	22.510 ± 0.280	−1.020
1433+553	Yes	16.810 ± 0.550	21.870 ± 0.710	73.920 ± 1.020	−2.197
1435+249(1)		9.210 ± 0.390	10.160 ± 0.500	11.800 ± 0.560	−0.270
2228−087		10.480 ± 0.312	11.190 ± 0.320	10.893 ± 0.670	0.049
2333+208(1)		6.601 ± 0.270	7.680 ± 0.290	11.410 ± 0.330	−0.714
2348+058		3.022 ± 0.240	3.400 ± 0.250	8.490 ± 0.290	−1.651
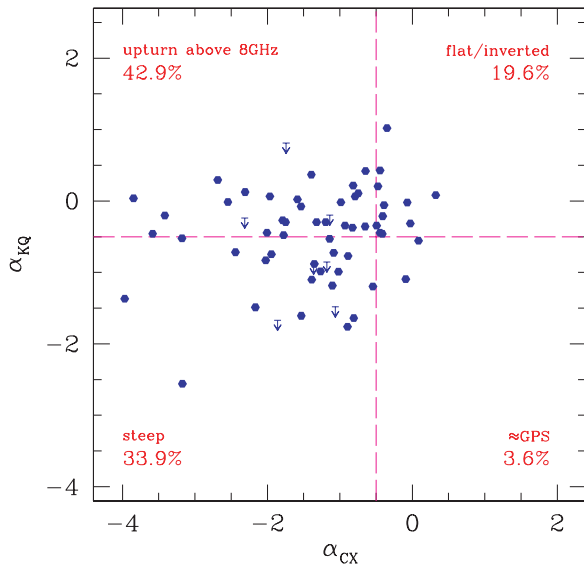
Figure 3. Distribution of the spectral indices provides a way to quantify the relative proportions of different spectral shapes, as indicated in the four quadrants. We list the percentage of each type of spectral shape in the corresponding quadrants. Note that a large fraction of sources exhibit curvature in their spectra (e.g., the "upturn" type).

(A color version of this figure is available in the online journal.)

Figure 4. Spectral index distribution in three frequency bands. The solid histogram is the result when only sources with core/pointlike morphology are used. The dashed histogram is obtained when all sources are included.

(A color version of this figure is available in the online journal.)

theirs. However, the fact that the two samples are selected at very different frequencies (1.4 GHz vs. 18 GHz) needs to be taken into consideration. In addition, although the majority of their sources are likely quasi-stellar objects (QSOs) and BL Lac objects, most of them lack redshift information, which makes it difficult to make a fair comparison (e.g., the nature of the sources and their environments, as well as possible cosmological evolution). Nevertheless, we agree with their conclusion that the extrapolation of fluxes to high frequencies (e.g., $\gtrsim 10$ GHz) based on low-frequency observations is not reliable.

6.6. Spectral Index Distribution

Here, we quantify the SIDs in the 5–8, 8–22, and 22–43 GHz bands. An important aspect in estimating the SIDs is to

deal with sources for which only an upper limit in flux in one of the bands is available, which leads to upper or lower limits of the spectral index. To accommodate such cases, we calculate the distribution with the ASURV package (Feigelson & Nelson 1985; Isobe et al. 1986), which is based on survival statistics, a branch of statistics developed on actuarial estimates of human survival and mortality (see, e.g., Feigelson & Nelson 1985 for a review). The resulting SIDs are shown in Figure 4, where the solid histogram is for sources with core/pointlike morphology, and the dashed histogram is for all sources. We record the mean values of the indices in Table 5. As expected, the SIDs based on all the sources have a mean that is more negative.

A recent study presents the spectral indices between 1.4 and 28.5 GHz for 95 probable cluster radio sources (Coble et al. 2007). They find that the mean of the index is ∼−0.7. Because of the differences between the beam size of the 1.4 GHz

Table 5
Mean Spectral Indices

Bands	All Sources	Cores/Pointlike
$5-8$	-1.64 ± 0.10	-1.31 ± 0.10
$8-22$	-1.20 ± 0.07	-0.88 ± 0.09
$22-43$	-0.98 ± 0.11	-0.62 ± 0.10

observations made by Ledlow & Owen (1996) and ours, we do not attempt to calculate an analog to their spectral index (e.g., α_{LK}). Furthermore, as the spectral shape tends to be complicated, it is not clear how much predictive power an index spanning such a wide range in frequency would have.

7. CORRELATION OF SPECTRAL INDICES AND PROPERTIES OF THE HOST GALAXIES AND CLUSTERS

Next, we examine if there is any correlation between the spectral indices (from sources of core/pointlike morphology) and the properties of the host galaxies or of the clusters. In particular, we consider the optical and radio luminosities, as well as the optical color, of the host galaxies. As for the cluster-related properties, we look at the mass and redshift of the clusters, and the projected radial distance to the cluster center, which is determined from the emission peak of the intracluster gas.

In Figure 5, we show scatter plots between α_{CX}/α_{KQ} and the galaxy properties. Figure 6 is the corresponding plot for the cluster properties. A few points are worth commenting on both figures. First, we note that the host galaxies are of moderate optical luminosity (recall that $M_* = -20.8$ in the V band), and are red in color ($u - r > 2.2$). Inspecting the optical images of the host galaxies from SDSS confirms that most of the galaxies are early type, of elliptical morphology. The distribution of the 1.4 GHz luminosities ($P_{1.4}$) suggests that these galaxies are likely FRI-type radio-loud AGNs.

The cluster mass M_{200} is estimated from the X-ray luminosity (L_X)–virial mass relation (Reiprich & Böhringer 2002). M_{200} is defined as the mass enclosed by r_{200}, a radius within which the mean overdensity is 200 times the critical density. Because of the scatter in the L_X–M_{200} relation, our mass estimate is only accurate to $\lesssim 50\%$ (Reiprich & Böhringer 2002). Nevertheless, it is shown that L_X is an unbiased mass indicator (Reiprich 2006). As our main purpose is to find correlations with the cluster mass, L_X should suffice as a proxy for mass. For each radio source, we normalize its clustercentric distance by r_{200}, to account for the difference in cluster mass. As Figure 6 suggests, our clusters span a range greater than 20 in mass. The majority of the sources are concentrated toward the cluster center, which confirms several earlier findings (e.g., Morrison & Owen 2003, LM07).

It is interesting to see that there appears to be no strong correlations between the spectral indices and the host galaxies/clusters. The Spearman's rank correlation coefficients for all cases we examine are between -0.1 and -0.34, indicating no significant correlations. The pair of properties that shows the strongest correlation is that between α_{KQ} and $P_{1.4}$ (correlation coefficient $= -0.34$). But this is mainly driven by a couple of sources that have the most negative spectral index.

Coble et al. (2007) do not find any difference between the spectral indices for sources in the inner and those in the outer parts of the clusters, suggesting a lack of correlation with clustercentric distance, which is consistent with our finding

here. Considering the fact that spatial distribution of the low-power radio galaxies is very concentrated toward cluster center (LM07), this seems to suggest that although being near the center of massive halos increases the probability of accretion onto the supermassive blackholes (e.g., high gas density or/and pressure from the ICM), the resulting emission is dominated by the small-scale physics of the nucleus rather than by the cluster environment.

8. IMPLICATIONS FOR SZE SURVEYS

The main motivation to conduct the present study is to characterize the SED/SID of radio sources associated with galaxy clusters, which can be used to assess their effect on the detection and characterization of clusters through the SZE. Simply put, the SIDs can be used to extrapolate the observed RLF at low frequencies to the frequency of an SZE experiment, which in turn provides an estimate of the abundance of radio sources.

Our approach is similar to that of LM07, and we refer the reader to that paper for more details (Section 7 therein). We will only provide an overview of the method here. The basic idea is to use the (observed) RLF within clusters and groups to predict the number and flux of radio sources expected in massive halos of given mass and redshift. Specifically, the RLF gives the number density of radio sources which, when multiplied by the volume of the halo, becomes the number of sources expected. One can draw (Poisson) random numbers from it, and assign radio luminosities according to the RLF. On the other hand, given the mass and redshift of a halo, one can predict its SZE signal, which can be compared with the total fluxes from the radio sources. By repeating this procedure for a large number of halos of the same mass and redshift, one produces a radio galaxy catalog in a Monte Carlo fashion, and can determine the fraction of clusters that are significantly affected by the radio sources they host. In Section 8.1, we describe our scheme for extrapolating the RLFs, and in Section 8.2, we present our estimates of the contamination of the SZE due to cluster radio sources.

8.1. Extrapolation of the Radio Luminosity Function

The main ingredients in our method include: the 1.4 GHz RLF of radio sources residing in massive halos, the SIDs between several frequencies, and a model for the redshift evolution of the RLF. The 1.4 GHz RLF in units of space density is measured in LM07, and we give in Section 7 the distributions for α_{CX}, α_{XK}, and α_{KQ}. For SZE surveys operating at $\sim$150 GHz (e.g., ACT and SPT), for low-redshift sources, our modeling requires a factor of $\sim$4 extrapolation of the radio spectra in frequency (i.e., from 43 GHz), which represents a dramatic improvement from that of LM07, which adapted an SID from 1.4 and 4.85 GHz measurements. However, because of the mismatch between the angular resolutions in our images at the C, X, and K bands, the spectral indices we determine between these bands may be lower limits, and thus the SIDs of α_{CX} and α_{XK} may be biased toward negative values. To assess the effects of the choices of SIDs, we will utilize other data sets to determine the SIDs at $\nu \lesssim 20$ GHz. To this end, we combine the catalogs from the NVSS (Condon et al. 1998) and GB6 (Gregory et al. 1996) surveys to measure the 1.4–4.85 GHz SID, and use the results from the AT20G survey (Sadler et al. 2006) to measure the 8.5–20 GHz SID. We describe the construction of the matched NVSS/GB6 sample, as well as the AT20G data,
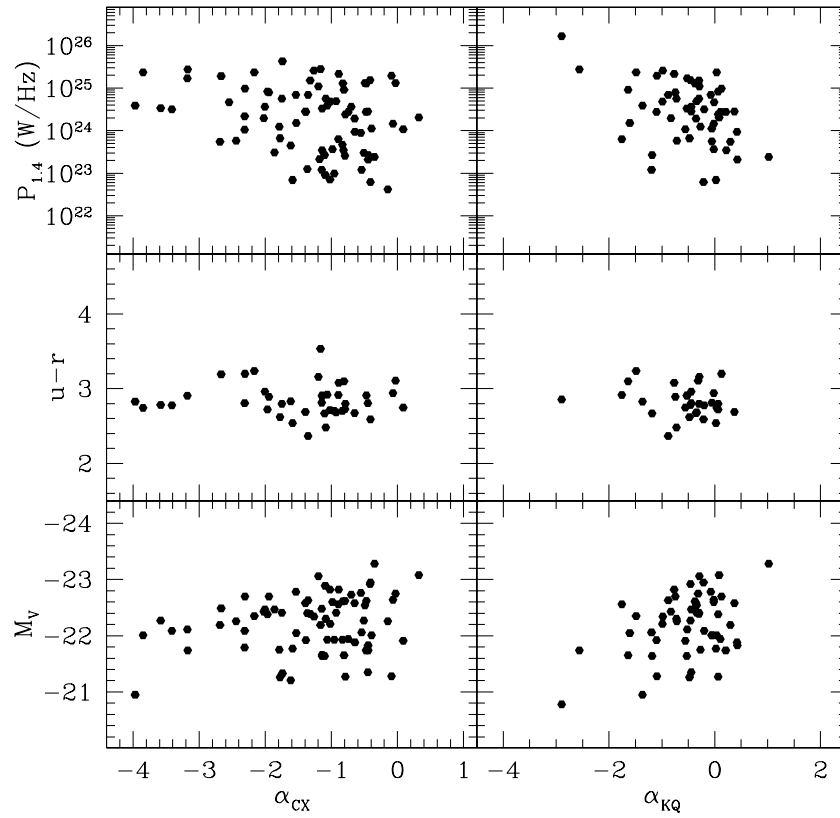
Figure 5. Distribution of the spectral indices with respect to properties of host galaxies. We consider the absolute optical (*V*-band) magnitude, the optical color (*u*−*r*), and the radio power at 1.4 GHz of the hosts. No apparent correlation is found.
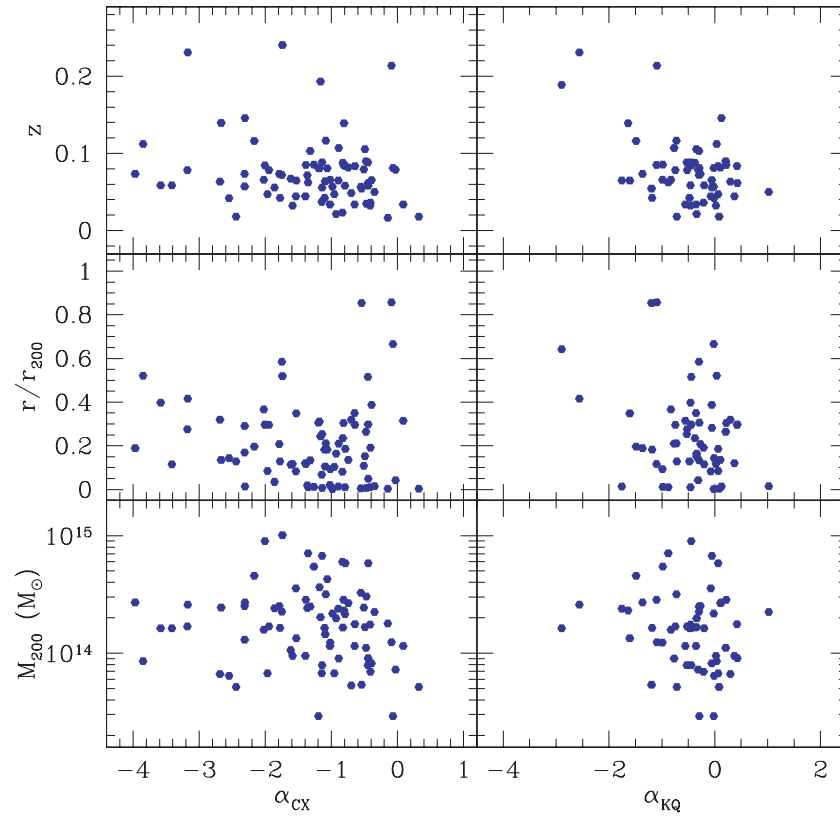
Figure 6. Distribution of the spectral indices with respect to properties of host clusters. We examine the mass of the clusters, the distance to the cluster center (normalized by the virial radius of the cluster, r_{200}), and the redshift. As expected, radio sources concentrate toward cluster center. As in Figure 5, we do not find significant correlations.

(A color version of this figure is available in the online journal.)
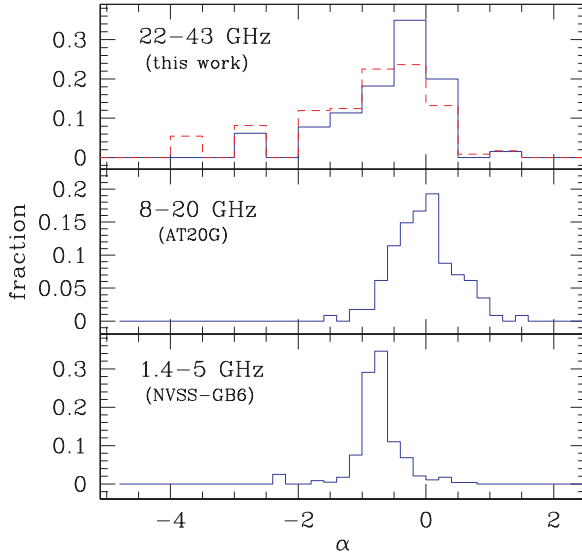
Figure 7. Spectral index distribution in three frequency bands. Top: the SID in the 22–43 GHz band as determined from our VLA data; this is identical to that shown in the top panel of Figure 4. Middle: the 8–20 GHz SID determined from the AT20G survey, using the data presented in Sadler et al. (2006). The mean of the distribution is $\alpha_{XK,\mathrm{AT20G}} = -0.028 \pm 0.046$. Bottom: the 1.4–5 GHz SID based on data from the NVSS and GB6 surveys. The mean is $\alpha_{LC,\mathrm{NVSS/GB6}} = -0.754 \pm 0.024$. The details of the construction of SID (8–20, AT20G) and SID (1.4–5, NVSS/GB6) are described in the Appendix. Compared to the middle and bottom panels in Figure 4, the SIDs in this figure are more positive. In particular, as AT20G is a 20 GHz-selected survey, the resulting SID is biased toward flat-spectrum sources.

(A color version of this figure is available in the online journal.)

in the Appendix. As the beam sizes of both NVSS and GB6 surveys are large (45″ and 3′.5, respectively), the flux, and in turn the spectral index α_{LC} measurements, should be reliable except for very extended sources. On the other hand, the AT20G survey selects sources at 20 GHz, and the resulting sample would be biased toward flat-spectrum sources. These SIDs are shown in the middle and lower panels in Figure 7. The mean values of $\alpha_{LC,NVSS/GB6}$ and $\alpha_{XK,AT20G}$ are -0.754 ± 0.024 and -0.028 ± 0.046, respectively. Using the SID (1.4–4.85, NVSS/GB6) and SID (8–20, AT20G) rather than those presented in Section 7 will produce extrapolated RLFs with higher amplitude (i.e., more radio sources), resulting in higher estimates of the contamination of SZE signals. We caution that the SIDs from NVSS/GB6 and AT20G are not limited to radio sources in groups and clusters[15] (although the NVSS/GB6 sources are constrained to be at $z < 0.4$). However, incorporating these SIDs allows us to explore the degree of AGN contamination of the SZE to a fuller extent.

LM07 measure the 1.4 GHz RLF for cluster radio sources. We transform that RLF to higher frequencies by convolving it with the spectral index distribution via (LM07)

$$\phi_2 \left(\log P_2 \right) = \int \phi_1 \left(\log P_2 + \alpha \log(\nu_1/\nu_2) \right) f(\alpha_{12}) d\alpha_{12}, \quad (1)$$

where $\phi \equiv dn/d \log P$ is the RLF, and the subscripts refer to two frequencies 1 and 2 ($\nu_2 > \nu_1$). The function $f(\alpha_{12})$ is the SID between the two frequencies. We have measured SIDs in several frequency bands: 1.4–5, 5–8, 8–20 (or 8–22), and 22–43.

---
[15] We note that radio-loud AGNs are known to reside in halos more massive than $\sim 10^{13}\,M_\odot$ or so (i.e., groups and cluster scale halos), based on their clustering properties (Mandelbaum et al. 2009; Wake et al. 2008).

Depending on the frequency of the SZE experiment, we may need to apply Equation (1) in several steps. For example, the RLF at 5 GHz is obtained by extrapolating the 1.4 GHz RLF with $f(\alpha_{1.4,5})$, and can be used in conjunction with $f(\alpha_{5,8})$ to obtain the 8 GHz RLF. Convolving the latter with $f(\alpha_{8,20})$ [or $f(\alpha_{8,22})$] gives the RLF at 10–30 GHz range. Finally, RLFs at higher frequencies (e.g., 145 GHz) are obtained by extrapolating the 22 GHz RLF with $f(\alpha_{22,43})$.

It is certainly preferable to utilize the full spectral shape from 5 to 43 GHz of our sources for the extrapolation of the RLFs. We elect not to do so in the current analysis, as our determination of the spectral shape below 22 GHz may not be reliable. Instead, we treat the spectral indices at different frequency bands as independent, and extrapolate the RLFs in a piecewise fashion. This is justified given the lack of correlation of spectral indices in the radio two-color diagram (Figure 3).

Ideally, one would extrapolate the RLF separately for the compact and extended components of radio sources. However, the 1.4 GHz RLF presented by LM07 is based on fluxes from both the core and extended structures. Given that at low frequencies, the lobes usually dominate in flux over the cores (e.g., Figure 2), the core-only RLF would have a smaller amplitude than the combined RLF. However, to determine the relative proportion of the core-only and the lobe-only RLFs, one needs to carefully examine all radio sources that contribute to the RLF, which is beyond the scope of the current analysis.

We note that the SID (1.4–4.85) derived from the NVSS/GB6 surveys should be representative for all sources with $\alpha_{1.4,4.85} \gtrsim -2$ (see the Appendix), and therefore may result in an extrapolation of the 1.4 GHz RLF (to $\sim$5 GHz) that appropriately takes into account the differences in the spectral shape of extended and compact sources. To further extrapolate to higher frequencies, we can use SIDs that are known to be biased toward positive and negative values of spectral indices, thus giving the (presumably) full range of possible RLFs. Our forecasts on the radio-source contamination of the SZE based on the RLFs will then reflect the incomplete knowledge of the source spectral shapes. To this end, for the four frequency ranges that we have determined the SIDs, we will employ a variety of SIDs to extrapolate the RLFs.

1. 1.4–5 GHz: SID (1.4–4.85, NVSS/GB6).
2. 5–8 GHz: SID (1.4–4.85, NVSS/GB6), SID (5–8, this work, point/corelike sources), or SID (5–8, this work, all sources).
3. 8–22 GHz: SID (8–22, this work, all sources) or SID (8–20, AT20G).
4. 22–43 GHz: SID (22–43, this work, point/corelike sources) or SID (22–43, this work, all sources).

8.2. Results

As explained in the previous subsection, using various combinations of SIDs we estimate the possible range of the RLFs given the uncertainties in the spectral shape of the radio sources. The $z \sim 0$ extrapolated RLFs (within r_{200}) at the four frequencies are shown as the shaded regions in Figure 8. The bottom (top) panel shows the RLFs at 15 and 30 GHz (90 and 145 GHz). At each frequency, the shaded region encloses the maximum and minimum of the RLFs resulted from the 12 SID combinations (six for 15 GHz). For comparison, in both panels the solid curve is the 1.4 GHz RLF.

Compared to a similar plot presented in LM07 (Figure 13 therein), a dramatic change in the amplitudes of the extrapolated
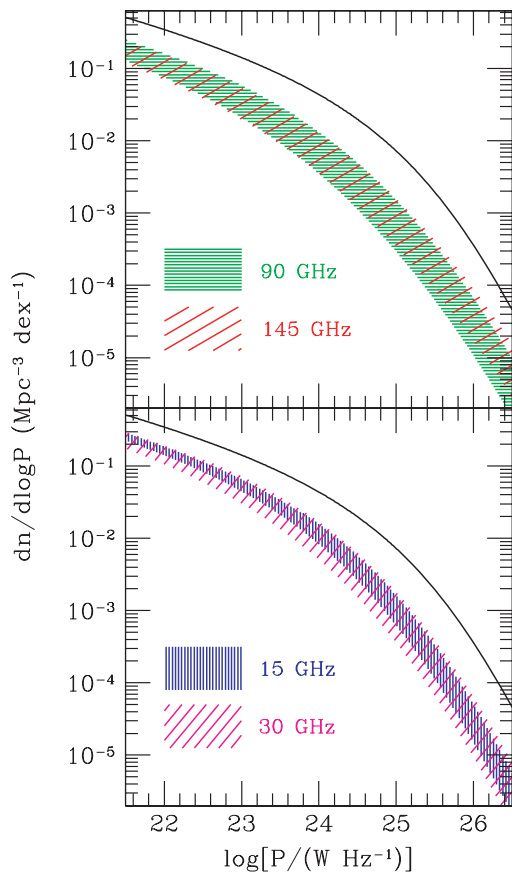
Figure 8. RLF of radio-loud AGNs at four frequencies. We transform the 1.4 GHz cluster AGN RLF from LM07 (measured within the virial radius; solid line) to 15 and 30 GHz (bottom panel), and 90 and 145 GHz (top panel), using Equation (1). To account for uncertainties in the spectral shapes of the sources, we use a variety of SIDs (see Section 8.1) to extrapolate the RLF; the shaded regions enclose the probable range of the RLFs at these frequencies.

(A color version of this figure is available in the online journal.)

RLFs is seen. At 145 GHz, at the luminous end, the upper envelop of the RLF is about a factor of 60 less than that estimated in LM07. This is due to the combined effect of (1) the use of several SIDs in different frequency bands in the present analysis (so that the results are not strongly dependent on one single SID), and (2) that the SID used in LM07 may be biased to positive indices, as nondetections at 4.85 GHz during the matching of sources between 1.4 and 4.85 GHz were not properly taken into account (see the Appendix for more discussion).

To check our extrapolation scheme, we show in Figure 9 a comparison between our extrapolated and the observed RLFs at 28.5 GHz, using data from Coble et al. (2007). We restrict ourselves to sources in the 37 clusters in the Coble et al. (2007) sample which have redshifts in the range 0.1–0.3, and for which X-ray observations are available, in order to match the selection criteria for our sources. Next, as the Coble et al. (2007) observations are made at the Berkeley–Illinois–Maryland Association (BIMA) and Owens Valley Radio Observatory (OVRO) arrays, we need to take account of the primary beam size of these arrays (6$'$.6 and 4$'$.2, respectively). We therefore include only the 27 radio sources that fall inside a projected radius of $r_{2000} \approx 0.33 r_{200}$, as this radius roughly matches the FWHM beam of BIMA for clusters in the redshift range 0.1–0.3. Using the source counts at 30 GHz from Knox et al. (2004), we estimate that roughly 11 sources could be background objects.
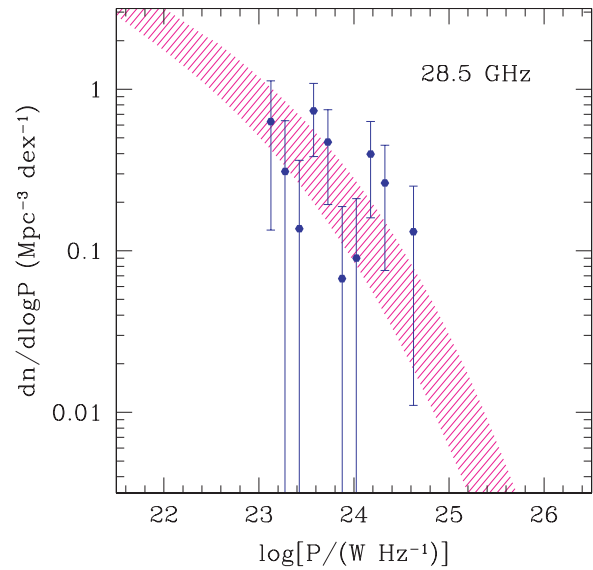
Figure 9. Comparison of our extrapolated RLF (shaded region) at 28.5 GHz with observations (points), for sources within r_{2000} (about 1/3 of the virial radius, r_{200}) in 37 clusters at $0.1 \leqslant z \leqslant 0.3$. The data is taken from Coble et al. (2007). Note that the extrapolated RLFs shown in Figure 8 are for regions within r_{200}; for comparison with observations restricted to $r_{2000} \approx r_{200}/3$, we have scaled the 28.5 GHz RLF within r_{200} by a constant factor that takes into account the different spatial distribution of mass and radio sources (assuming that the two components follow the Navarro et al. 1997 profile with concentration of 5 and 30, respectively).

(A color version of this figure is available in the online journal.)

Given this uncertainty and the small number of sources, the RLF is not well determined. Furthermore, it is difficult to evaluate the impact of the Coble et al. (2007) cluster selection on the resulting RLF (if anything, the amplitude of the RLF should be higher, because their cluster sample is selected *against* those hosting bright point sources). Nevertheless, it is reassuring to find that there is a general agreement between the data points and our extrapolation (shaded region).

We note that the redshift evolution of radio sources in clusters is an unresolved issue. Our sample is limited to $z < 0.25$, and currently there is no consensus as how radio galaxies evolve in massive halos (see LM07 for discussion). We have acquired C-, X-, and K-band data for a sample of radio galaxies in $\sim$10 intermediate-redshift clusters. Better constraints on the redshift evolution based on these new data will be presented in a future publication. In the current analysis, we will assume a pure density evolution of the form $\phi(z) \propto \phi(z = 0)(1 + z)^\gamma$, with $\gamma = 1$, which corresponds to a factor of 2 increase of the density at $z \approx 1$. Such an evolution is derived from an analysis of the cluster radio source evolution from the Red-Sequence Cluster Survey (M. Roscioli & M. D. Gladders 2009, in preparation; M. Gladders 2008, private communication), and is much milder than what is assumed in LM07. The contamination of the SZE due to radio sources based on the present analysis is therefore much smaller when compared to the forecast presented in LM07.

Now, given the mass and redshift of a dark matter halo, we can estimate the degree of contamination as follows. For a halo, we denote the total fluxes from radio sources as S_{AGN}, and the SZE signal as S_{SZE}. Using our Monte Carlo scheme to generate a large number of radio sources in massive halos, the fraction of halos for which S_{AGN} is a significant fraction q of $|S_{SZE}|$ can be calculated. We consider two cases, $q = 0.2$ and $q = 1$, corresponding to 20% and 100% contamination. We show in
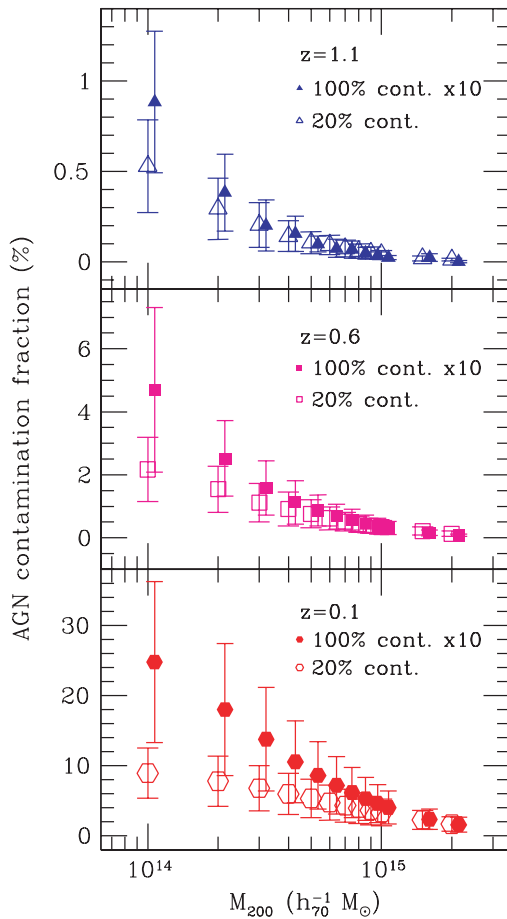
Figure 10. Fraction of clusters which host enough radio-loud AGNs such that their SZE signal measurements at 145 GHz may be contaminated. We consider cases where the fluxes of the AGNs are at least a fraction q of the SZE signal, $S_{\mathrm{AGN}} \geqslant q|S_{\mathrm{SZE}}|$ (for the case where SZE signal is a temperature decrement), with $q = 0.2$ (open symbols) and $q = 1$ (solid symbols). Note the $q = 1$ contamination fraction is multiplied by a factor of 10 for clarity of presentation. From bottom to top we examine clusters at $z = 0.1, 0.6$, and 1.1. A mild density evolution of the radio sources is assumed (corresponding to a factor 2 increase at $z = 1$ compared to $z = 0$). The contamination fraction is quite small (always $<10\%$), and decreases with both cluster mass and redshift. The error bars show the 1σ range of possible degrees of contamination, reflecting our incomplete knowledge of the spectral shape of the radio sources.

(A color version of this figure is available in the online journal.)

Figure 10 the resulting AGN contamination fraction (ACF) at 145 GHz, which is the proportion of the clusters expected to host radio galaxies whose flux is $S_{\mathrm{AGN}} \geqslant q|S_{\mathrm{SZE}}|$, as a function of cluster mass. The three panels show the results at $z = 0.1$, 0.6, and 1.1 (bottom to top). In each panel, the open points refer to the case of $q = 0.2$, while the solid points show the $q = 1$ ACF multiplied by a factor of 10 (for better presentation). Using different combinations of SIDs, we have constructed 12 145 GHz RLFs, resulting in a range of degree of contamination (at a given halo mass and redshift). While the points show the mean value of the contamination fractions, the error bars indicate the 1σ range based on the 12 estimates.

The general trend shown in Figure 10 is that the ACF decreases as cluster mass and redshift increase. For $q = 0.2$ contamination, the most affected clusters are those nearby, at $\sim 10\%$ level for $M_{200} = 10^{14}$ $M_\odot$ clusters, reaching to 1%–2% for $M_{200} \geqslant 10^{15}$ $M_\odot$ ones. At $z = 0.6$, an epoch close to the peak of cluster redshift distribution, the $q = 0.2$ ACF is reduced to $<2\%$ at 10^{14} $M_\odot$, and becomes negligible toward

the high-mass end. At $z = 1.1$ the $q = 0.2$ ACF is always at subpercent level. Finally, the proportion of clusters that are affected by AGNs to 100% is a factor of 4–5 smaller than the above estimates. For completeness, we note that about 0.4%–4% (1%–7%) of clusters in the mass range 10^{14}–10^{15} $M_\odot$ at $z \sim 0.6$ may be contaminated to 10% (5%) level (i.e., $q = 0.1$ and 0.05, respectively). At $z = 1.1$, these values become 0.04%–1% (0.2%–2%).

We have provided a framework for estimating the abundance of radio-loud AGNs in halos. To better determine the impact of radio sources in SZE surveys, however, it is necessary to carry out mock observations that take into account the properties of the telescope and receiver system (e.g., angular resolution, sensitivity, frequency; see Sehgal et al. 2007), as well as the auxiliary observations (e.g., availability of multiwavelength data).

9. SUMMARY AND FUTURE WORK

We have presented a study of the SED of radio sources in a large sample of nearby clusters ($z < 0.25$). For 139 sources selected at 1.4 GHz and spectroscopically confirmed to be the members of the clusters, we use the VLA to measure the flux densities at 4.9, 8.5, 22, and 43 GHz (C, X, K, and Q bands) nearly simultaneously, and determine the distribution of the SED. Sources with extended morphology may be resolved out at high frequencies (i.e., reduction in flux due to the higher angular resolution of interferometer), making the determination of the spectral shape nontrivial. We have downgraded the resolution of our 43 GHz images to match the resolution at 22 GHz, thus enabling reliable comparisons of fluxes at these two frequencies (Section 5.1); it is more difficult to match the resolution between the other frequency intervals, and therefore our measurements of the spectral indices involving the two lower frequencies (e.g., between 8.5 and 22 GHz, α_{XK}, where $S \propto \nu^\alpha$) are *lower* limits. The flux measurement of pointlike (or barely resolved) sources, or "cores" embedded in extended sources, on the other hand, is more straightforward.

Our main findings are the following.

1. For ~ 70 core/pointike sources that are detected in at least three frequencies, we study the distribution of the spectral shape via the "two-color" diagram (Figure 3), and find that the spectral shape cannot be described by simple power laws for the bulk of the sources. About 60% of the sources have $\alpha_{KQ} > \alpha_{CX}$, indicating a flattening of the spectral shape above 8 GHz or so; only 1/3 of the sources have steep spectra in the entire range from 4.9 to 43 GHz.

2. We determine the spectral index distribution using survival statistics that take nondetections (upper limits) into account. The results are shown in Figure 4 and Table 5. The compact sources are found to have "flatter" spectral shape than the extended sources.

3. The spectral indices do not correlate with properties of host galaxies or clusters, such as the color and luminosity of the galaxies, the radio luminosity at 1.4 GHz, the distance of the host galaxy to the cluster center, and the mass of the host clusters. This result agrees with previous studies, and suggests that the radio emission may be dominated by the small-scale physics of the nucleus, rather than by the cluster environment.

4. In an attempt to estimate the contamination of the SZE signal due to radio point sources in cluster surveys, we make use of the spectral index distributions in several frequency

bands to extrapolate the well measured RLF at 1.4 GHz to the frequencies employed by several ongoing radio/ millimeter wave experiments. As the extrapolation depends on the SIDs employed, we bracket the possible range of the predicted RLFs by using SIDs in intermediate frequency bands (e.g., 8–20 GHz) that are known to be biased in opposite ways. The amplitude of the resulting RLFs at $\nu \geqslant 30$ GHz is in general 5–20 times lower compared to that at 1.4 GHz. Under the assumption that the RLF follows a pure density evolution with redshift of the form $\phi(z) \propto \phi(z=0)(1+z)^\gamma$, such that the abundance of sources at $z = 1$ is twice the local value, we find that the fraction of clusters that may be seriously affected by point sources is quite small; at the cluster mass scales close to the detection limits of the ongoing surveys (e.g., $(2–3) \times 10^{14}\ M_\odot$), and at the redshift where we expect the experiments to detect most of the clusters (i.e., $z \sim 0.6$), $\lesssim 2\%$ of the clusters will be contaminated to 20% level or above (that is, the total fluxes from AGNs are at least 20% of the SZE signal).

There are two aspects that need to be improved for a better forecast within our analysis framework. Currently, the largest uncertainty in our modeling is the redshift evolution of cluster radio galaxies. If not properly accounted for, any unexpected evolution of the radio sources may be misinterpreted as changes in the cluster mass function, and cause errors in the determination of the properties of the dark energy. With our ongoing VLA survey of cluster radio galaxies at intermediate redshift ($0.3 \leqslant z \leqslant 0.8$), we plan to address this issue in a future publication.

In addition, in our forecast, it is implicitly assumed that the number of radio galaxies (N_{RG}) a cluster can host is proportional to the cluster mass (M_{200}). If, instead, $N_{RG} \propto M_{200}^s$ with $s < 1$, we would overestimate the AGN contribution in high-mass clusters. To check this assumption, one needs to determine the halo occupation distribution for radio galaxies. To this end, we have attempted to construct the halo occupation distribution of radio galaxies, using a large sample of radio galaxies in the local universe (Y. T. Lin et al. 2009, in preparation).

Mainly because of the very mild redshift evolution of the radio sources we adopt (which is based on the results from the RCS survey; M. Roscioli & M. D. Gladders 2009, in preparation), we find that radio sources do not cause a substantial degree of contamination to the SZE signal. To control the systematics in the ongoing and future SZE cluster surveys, it is thus crucial to understand the contamination due to the dusty IR sources. Rapid progress has been made on this regard (e.g., Righi et al. 2008; Fernandez-Conde et al. 2008). It would be important to perform an assessment of contamination due to both radio and IR sources within a single framework, which is the goal of our research in the near term.

APPENDIX

SPECTRAL INDEX DISTRIBUTIONS FROM NVSS/GB6 AND AT20G SURVEYS

Here, we describe the construction of the spectral index distributions, SID (1.4–5, NVSS/GB6) and SID (8–20, AT20G), as shown in Figure 7.

The NRAO VLA Sky Survey (NVSS; Condon et al. 1998) is a 1.4 GHz survey covering the sky north of $\delta = -40°$, with a resolution of 45″. The nominal detection limit is 2.5 mJy. The Green Bank 4.85 GHz (GB6) survey (Gregory et al. 1996) used NRAO's (former) 91 m telescope to survey the sky within $0° < \delta < 75°$, with a resolution of 3′.5, and a detection threshold of 18 mJy. We first match the NVSS source catalog to the spectroscopic sample of SDSS DR6 (with a conservative matching radius of 10″), and limit the combined sample to $z < 0.4$, as we are interested in the radio galaxies in the local universe. We then cross-correlate the NVSS/SDSS sample with GB6 (again using a conservative matching radius of 1′), keeping all unmatched NVSS/SDSS sources (for which we can derive upper limits on α_{LC}). Because of the differences in the angular resolution of the two radio surveys, we further limit ourselves to NVSS sources for which there are no neighboring sources from NVSS within a radius of 4′. This is to ensure that both surveys measure the "total" flux from the sources, and to avoid sources that might be blended in the lower resolution GB6 survey. Finally, to account for the differences in the detection limits, we set a high flux cut (100 mJy) for NVSS sources so that we can be sure to include all sources with $\alpha_{LC} > -1.4$. Of the resulting 292 NVSS sources, nine are not detected in GB6, and we assign 18 mJy as the upper limit in the 4.85 GHz flux for these sources. The SID from this sample is shown in the lower panel in Figure 7. We note that our result is not sensitive to the flux cut applied to the NVSS sources or on the requirement

for the "isolatedness" of the sources. Neither setting the cut to 200 mJy (so that we are complete for sources with $\alpha_{LC} > -1.9$) nor including sources with neighbors closer than $4'$ changes the mean value of the SID beyond the 1σ level.

The ATCA is conducting a large survey at 20 GHz (AT20G) that will eventually cover the sky south of $\delta = 0°$. A bright source catalog based on observations up to 2004 is reported by Sadler et al. (2006). We use the 114 sources stronger than 100 mJy at 20 GHz that are also detected at 8.6 GHz to construct the SID, and show the result in the middle panel of Figure 7. Because the sources are selected at 20 GHz, the SID is biased toward positive values. Furthermore, the redshifts for the majority of the sources are not available, and thus the result may not be representative of the rest-frame 8–20 GHz SID. Nevertheless, this sample provides a distribution that is at the opposite extreme compared to that from our VLA observations, and therefore the two SIDs should bracket the true distribution.

REFERENCES

Abell, G. O. 1958, ApJS, 3, 211
AMI Collaboration 2006, MNRAS, , 369, L1
Bolton, R. C., et al. 2004, MNRAS, 354, 485
Carlstrom, J. E., Holder, G. P., & Reese, E. D. 2002, ARA&A, 40, 643
Coble, K., et al. 2007, AJ, 134, 897
Condon, J. J., Cotton, W. D., Greisen, E. W., Yin, Q. F., Perley, R. A., Taylor, G. B., & Broderick, J. J. 1998, AJ, 115, 1693
Cooray, A. R., Grego, L., Holzapfel, W. L., Joy, M., & Carlstrom, J. E. 1998, AJ, 115, 1388
de Young, D. S. 2002, The Physics of Extragalactic Radio Sources (Chicago, IL: Univ. Chicago Press)
de Zotti, G., Ricci, R., Mesa, D., Silva, L., Mazzotta, P., Toffolatti, L., & González-Nuevo, J. 2005, A&A, 431, 893
Feigelson, E. D., & Nelson, P. I. 1985, ApJ, 293, 192

Fernandez-Conde, N., Lagache, G., Puget, J.-L., & Dole, H. 2008, A&A, 481, 885
Fowler, J. W., et al. 2007, Appl. Opt., 46, 3444
Gregory, P. C., Scott, W. K., Douglas, K., & Condon, J. J. 1996, ApJS, 103, 427
Isobe, T., Feigelson, E. D., & Nelson, P. I. 1986, ApJ, 306, 490
Knox, L., Holder, G. P., & Church, S. E. 2004, ApJ, 612, 96
Ledlow, M. J., & Owen, F. N. 1995, AJ, 109, 853
Ledlow, M. J., & Owen, F. N. 1996, AJ, 112, 9
Lima, M., & Hu, W. 2005, Phys. Rev. D, 72, 043006
Lin, Y.-T., & Mohr, J. J. 2003, ApJ, 582, 574
Lin, Y.-T., & Mohr, J. J. 2007, ApJS, 170, 71
Mandelbaum, R., Li, C., Kauffmann, G., & White, S. D. M. 2009, MNRAS, 393, 377
Miller, N. A., & Owen, F. N. 2001, ApJS, 134, 355
Morrison, G. E., & Owen, F. N. 2003, AJ, 125, 506
Navarro, J. F., Frenk, C. S., & White, S. D. M. 1997, ApJ, 490, 493
Owen, F. N., & Ledlow, M. J. 1997, ApJS, 108, 41
Owen, F. N., Ledlow, M. J., & Keel, W. C. 1995, AJ, 109, 14
Pierpaoli, E., & Perna, R. 2004, MNRAS, 354, 1005
Reiprich, T. H. 2006, A&A, 453, L39
Reiprich, T. H., & Böhringer, H. 2002, ApJ, 567, 716
Righi, M., Hernández-Monteagudo, C., & Sunyaev, R. A. 2008, A&A, 478, 685
Ruhl, J., et al. 2004, in Proc. SPIE 5498, Millimeter and Submillimeter Detectors for Astronomy II, ed. J. Zmuidzinas, W. Holland, & S. Withington (Bellingham, WA: SPIE), 11
Sadler, E. M., Ricci, R., Ekers, R. D., Sault, R. J., Jackson, C. A., & de Zotti, G. 2008, MNRAS, 385, 1656
Sadler, E. M., et al. 2006, MNRAS, 371, 898
Sehgal, N., Trac, H., Huffenberger, K., & Bode, P. 2007, ApJ, 664, 149
Staniszewski, Z., et al. 2008, ApJ, submitted (arXiv:0810.1578)
Sunyaev, R. A., & Zel'dovich, Y. B. 1970, Ap&SS, 7, 3
Toffolatti, L., Argueso Gomez, F., de Zotti, G., Mazzei, P., Franceschini, A., Danese, L., & Burigana, C. 1998, MNRAS, 297, 117
Wake, D. A., Croom, S. M., Sadler, E. M., & Johnston, H. M. 2008, MNRAS, in press (arXiv:0810.1050)
White, M., & Majumdar, S. 2004, ApJ, 602, 565
Zwart, A. C. J. T. L., et al. 2008, MNRAS, 391, 1545